

Worldline Monte Carlo for fermion models at large N_f

Gerald Dunne

Department of Physics, University of Connecticut, Storrs, CT 06269-3046, USA
E-mail: dunne@phys.uconn.edu

Holger Gies

Theoretisch-Physikalisches Institut, Friedrich-Schiller-Universität Jena, D-07743 Jena
& Institut für Theoretische Physik, Universität Heidelberg D-69120 Heidelberg, Germany
E-mail: holger.gies@uni-jena.de

Klaus Klingmüller

Institut für Theoretische Physik E, RWTH Aachen University, D-52056 Aachen
& Institut für Theoretische Physik, Universität Heidelberg D-69120 Heidelberg, Germany
E-mail: klingmueller@physik.rwth-aachen.de

Kurt Langfeld

School of Maths & Stats, University of Plymouth, Plymouth, PL4 8AA, England
E-mail: Kurt.Langeld@plymouth.ac.uk

ABSTRACT: Strongly-coupled fermionic systems can support a variety of low-energy phenomena, giving rise to collective condensation, symmetry breaking and a rich phase structure. We explore the potential of worldline Monte Carlo methods for analyzing the effective action of fermionic systems at large flavor number N_f , using the Gross-Neveu model as an example. Since the worldline Monte Carlo approach does not require a discretized spacetime, fermion doubling problems are absent, and chiral symmetry can manifestly be maintained. As a particular advantage, fluctuations in general inhomogeneous condensates can conveniently be dealt with analytically or numerically, while the renormalization can always be uniquely performed analytically. We also critically examine the limitations of a straightforward implementation of the algorithms, identifying potential convergence problems in the presence of fermionic zero modes as well as in the high-density region.

KEYWORDS: chiral fermions, low-dimensional models, Monte Carlo methods .

Contents

1. Introduction	2
2. Worldline representation of the effective action	3
2.1 Continuum formulation	3
2.2 Propertime discretization	4
2.3 Renormalization	5
3. Spatially inhomogeneous σ condensates	7
3.1 Worldline formalism	7
3.2 Single kink condensate	9
3.3 Kink-antikink pair condensate	11
3.4 Periodic array of kink-antikink pairs	13
3.5 Kink crystal condensate	18
3.6 Worldline ensembles from Hybrid Monte Carlo	18
4. Worldline approach at finite temperature and chemical potential	23
4.1 Temperature in the worldline representation	23
4.2 Chemical potential in the worldline representation	25
4.3 High densities and low temperatures	26
4.4 Crystalline phase on the worldline	28
5. Conclusions	29
A. Fermionic models and continuous chiral symmetry	30
B. Exact resolvents and propagators for $(1+1)$-dim. Gross-Neveu model	31
B.1 Homogeneous condensate	32
B.2 Single kink condensate	32
B.3 Kink-antikink pair condensate	32
B.4 Periodic array of kink-antikink pairs	33
B.5 Comparison with heat kernel expansion	33
C. Effective action for the homogeneous case	34

1. Introduction

The elaboration of the QCD phase diagram as a function of temperature and baryon density represents a great challenge in modern particle and nuclear physics. It has been studied experimentally at the RHIC collider at Brookhaven and at CERN. It has also attracted intense theoretical investigation using computer simulations in the context of lattice gauge theory and random matrix theory [1]. A significant computational obstacle is the so-called sign problem, for which a number of approximate techniques have been developed: (i) a Taylor expansion with respect to the baryon chemical potential [2, 3, 4]; (ii) imaginary values for the chemical potential μ [5, 6, 7]; (iii) overlap enhancing techniques [8]. Despite these impressive successes, our knowledge of the QCD phase diagram is still rather limited. Other approaches include the study of QCD-like theories such as 2-colour QCD [9, 10, 11], and high density quark matter in a colour superconducting state [12, 13, 14, 15, 16]. Of particular interest is the identification of inhomogeneous phases, analogous to the LOFF states of condensed matter systems [17, 18, 19, 16, 20]. This idea has been studied deeply for Skyrme models [21, 22, 23, 24], and for four-fermion models [25, 26, 20]. Lower dimensional models also provide insight into chiral dynamics, and early lattice studies of lower-dimensional models such as the Gross Neveu model in the limit of many flavours have shown that inhomogeneous background fields are key to understand the dense phase [27]. Recently, this model has attracted a lot of interest since it was found analytically that the high-density state of fermion matter forms an inhomogeneous “baryon crystal” [28, 29, 30, 31]. This analytic crystalline phase has been confirmed by a lattice analysis [32], and such studies have led to several new insights concerning inhomogeneous phases [33, 34].

Good chiral properties of the fermion action is of central importance for an investigation of quark matter at intermediate densities, since the high-density transition is driven by chiral dynamics. Unfortunately, lattice fermion actions necessarily suffer from the fermion doubling problem as firstly pointed out by Nielsen and Ninomiya [35]. Nowadays, staggered fermions [36], domain wall fermions [37] or Neuberger fermions [38], which are an explicit realization of the Ginsparg-Wilson relation [39], are widely used in numerical simulations. Despite these advanced formulations and great numerical efforts, it turns out still to be cumbersome to achieve good chiral properties, such as a sufficiently small pion mass.

Here we propose to use the *worldline* approach to study interacting fermion systems. Since the worldline approach to the quark determinant does not use a lattice discretization of space-time, it circumvents many of these significant difficulties. Here, we will argue that the prospects of the worldline approach are (i) exact chiral symmetry but yet a fully numerical approach, (ii) analytic renormalization and (iii) a clear description of Fermi surface effects. The worldline method is a string-inspired approach to quantum field theory; see [40, 41] for reviews. It was further developed into a viable tool for an efficient calculation of functional determinants for arbitrary background fields [42]. Subsequently, *worldline numerics* has enjoyed a wide span of applications ranging from the Casimir effect [43, 44] and fermion induced quantum interactions [45] to the description of pair production in inhomogeneous fields [46, 47]. A worldline lattice formulation has also been presented in [48].

In this paper we apply a worldline Monte Carlo approach to interacting fermion models, concentrating on the $(1+1)$ -dimensional Gross-Neveu model [49, 50]. We review these models in Section 2, and describe the worldline representation of the effective action. The treatment of inhomogeneous condensates is presented in Section 3, and the extension to finite temperature and chemical potential is explained in Section 3, along with results of the computations. Section 5 contains our conclusions, and several appendices contain relevant technical details.

2. Worldline representation of the effective action

2.1 Continuum formulation

In this work, we mainly concentrate on the $D = 1 + 1$ dimensional Gross-Neveu (GN) model defined by the Euclidean fermionic action [49, 50]

$$S_F = \int d^D x \left(-\bar{\psi} \not{\partial} \psi + \frac{g^2}{2N_f} (\bar{\psi} \psi)^2 \right), \quad (2.1)$$

where N_f denotes the number of flavors. The GN model has a discrete chiral symmetry under $\psi \rightarrow \gamma_5 \psi$. Our conventions for the Dirac algebra in $D = 1 + 1$ are $\gamma_1 = i\sigma_3$, $\gamma_2 = i\sigma_1$, $\gamma_5 = \sigma_2$, $\{\gamma_\mu, \gamma_\nu\} = -2\delta_{\mu\nu}$, but most of the equations below generalize straightforwardly to higher dimensions. With the aid of a Hubbard-Stratonovich transformation, we can rewrite this model in terms of a mixed fermionic-bosonic action

$$S_{FB} = \int d^D x \left[\frac{N_f}{2g^2} \sigma^2 - \bar{\psi} \not{\partial} \psi - i\sigma \bar{\psi} \psi \right] \quad (2.2)$$

with the bosonic scalar $\sigma(x)$ which transforms as $\sigma \rightarrow -\sigma$ under the discrete chiral symmetry. In this work, we actually confine ourselves strictly to the large- N_f limit of this model which is equivalent to a semiclassical approximation of the σ sector. Integrating out the remaining fermion fluctuations, results in the large- N_f effective action

$$\Gamma[\sigma] = \int d^D x \frac{N_f}{2g^2} \sigma^2 - N_f \text{Tr} \ln(-\not{\partial} - i\sigma), \quad N_f \rightarrow \infty. \quad (2.3)$$

The resulting Dirac operator $\mathcal{D} = i\not{\partial} - \sigma$ has a γ_5 hermiticity, $\mathcal{D}^\dagger = \gamma_5 \mathcal{D} \gamma_5$, implying that the fermionic contribution to Γ is real. In this case, we can use the identity $\text{Tr} \ln i\mathcal{D} = \frac{1}{2} \text{Tr} \ln \mathcal{D} \mathcal{D}^\dagger$ to obtain

$$\Gamma[\sigma] = \int d^D x \frac{N_f}{2g^2} \sigma^2 - \frac{N_f}{2} \text{Tr} \ln(-\partial^2 + \sigma^2 - i\not{\partial} \sigma), \quad N_f \rightarrow \infty, \quad (2.4)$$

now involving a fluctuation operator of Laplace type.

A variety of fermionic models of a similar type exist. An example for a model with a continuous chiral symmetry is given by the Thirring model which is discussed in appendix A. Here, we concentrate on the Gross-Neveu model. The contribution from the fermion fluctuations to the effective action can be written in proper-time form,

$$\Delta\Gamma[\sigma] := -\frac{N_f}{2} \text{Tr} \ln(-\partial^2 + \sigma^2 - i\not{\partial} \sigma) \quad (2.5)$$

$$= \frac{N_f}{2} \int_{1/\Lambda^2}^\infty \frac{dT}{T} \text{Tr} e^{-(\partial^2 + \sigma^2 - i\not{\partial} \sigma)T}, \quad (2.6)$$

where we have used a proptime UV cutoff Λ for the sake of definiteness; any other regularization scheme can similarly be implemented. Interpreting the fluctuation operator in the exponent as a quantum mechanical Hamiltonian H , we can introduce the path integral representation of the proptime evolution operator $\exp(-HT)$,

$$\Delta\Gamma[\sigma] = \frac{N_f}{2} \frac{1}{(4\pi)^{D/2}} d_\gamma \int_{1/\Lambda^2}^{\infty} \frac{dT}{T^{D/2+1}} \int_{x(0)=x(T)} \mathcal{D}x e^{-\frac{1}{4} \int_0^T d\tau \dot{x}^2(\tau)} e^{-\int_0^T d\tau \sigma^2} \Phi[\sigma], \quad (2.7)$$

containing the spin factor

$$\Phi[\sigma] = \frac{1}{d_\gamma} \text{tr}_\gamma \mathcal{P} \exp \left(i \int_0^T d\tau (\not{\partial} \sigma) \right), \quad (2.8)$$

and σ are functions of $x(\tau)$. The normalization of the path integral in Eq. (2.7) has been chosen such that $\int \mathcal{D}x \exp(-\int \dot{x}^2/4) = 1$. We also introduced the dimensionality of the Dirac algebra d_γ , e.g., $d_\gamma = 2^{D/2}$ in even dimensions, such that $\Phi[0] = 1$.

2.2 Propertime discretization

For a given background of arbitrarily varying σ and V fields, the analytic computation of the effective action Γ is formidable. For a numerical computation, the worldline representation is highly useful, since the computation of the path integral in Eqs. (2.7) or (A.5) can be done efficiently with Monte Carlo methods. Most importantly, the algorithm can be formulated for any background σ in full generality.

An estimate for the path integral over an operator $\mathcal{O}[x]$ is given by an average over a finite ensemble of closed worldlines (“loops”) $x_\ell(\tau)$, where $\ell = 1, \dots, n_L$.

$$\int_{x(0)=x(T)} \mathcal{D}x \mathcal{O}[x] e^{-\frac{1}{4} \int_0^T d\tau \dot{x}^2(\tau)} \equiv \langle \mathcal{O}[x] \rangle \simeq \frac{1}{n_L} \sum_{\ell=1}^{n_L} \mathcal{O}[x_\ell]. \quad (2.9)$$

Since the path integral is over all spacetime, it can be decomposed into a spacetime integral over a “center of mass” (CM) and a path integral over worldlines fixed to this common center of mass,

$$\langle \mathcal{O}[x] \rangle = \int d^D x_{\text{CM}} \langle \mathcal{O}[x] \rangle_{x_{\text{CM}}} \quad (2.10)$$

This latter ensemble of mass-centered worldlines x_ℓ is generated according to a Gaussian velocity distribution

$$P_{\text{CM}}[x] = \delta \left(x_{\text{CM}} - \int_0^T d\tau x(\tau) \right) e^{-\frac{1}{4} \int_0^T d\tau \dot{x}^2(\tau)}, \quad (2.11)$$

where the δ function implements the center-of-mass constraint. The center-of-mass integration relates the effective action with a corresponding action density, i.e., the Lagrangian, $\Gamma = \int d^D x_{\text{CM}} \mathcal{L}(x_{\text{CM}})$, but this decomposition of the worldlines is not unique. Alternatively, the worldlines in the ensemble can be fixed to have one common point (CP), say at $\tau = 0$,

$$P_{\text{CP}}[x] = \delta(x_{\text{CP}} - x(\tau = 0)) e^{-\frac{1}{4} \int_0^T d\tau \dot{x}^2(\tau)}, \quad (2.12)$$

such that $\langle \mathcal{O}[x] \rangle = \int d^D x_{\text{CP}} \langle \mathcal{O}[x] \rangle_{x_{\text{CP}}}$. The associated Lagrangian \mathcal{L} , $\Gamma = \int d^D x_{\text{CP}} \tilde{\mathcal{L}}(x_{\text{CP}})$, is not identical to the one related to the center-of-mass definition, but agrees with it up to a total derivative term [40]. Below, we use both prescriptions: whereas the CM worldlines have some computational advantages due to the constraint $\int x(\tau) = 0$, analytical results are often related to the representation involving CP worldlines.

The finite ensemble of worldline loops still has an infinite set of degrees of freedom. We reduce these to finitely many by a discretization of the proper-time coordinate τ , resulting in an approximation of each worldline by a finite set of N points per loop, $x_i := x(\tau_i)$, $\tau_i = Ti/N$, $i = 0, \dots, N$, where the points $x_{i=0} \equiv x_{i=N}$ are identified. Replacing the proper-time derivative in the worldline action by a nearest-neighbor difference, $\dot{x}(\tau_i) \rightarrow N(x_i - x_{i-1})/T$, leads to a Gaussian action for the x_i which can be diagonalized including the δ constraint. This allows for an ab-initio generation of a random worldline distribution; for concrete algorithms, see [43, 51]. A discretization in terms of Fourier modes is also possible and will be used in Sect. 3.6; it shows a slightly slower convergence towards the proper-time continuum limit [43].

Whereas the finiteness of the number of worldlines introduces an error which is measurable by the statistical error of the expectation values, the proper-time discretization leads to a systematic error which has to be studied by approaching the continuum limit, i.e., by increasing the value of N .

It should be stressed that only the auxiliary proper-time is discretized, whereas the spacetime coordinates remain continuous, $x_i \in \mathbb{R}^D$ (at least to machine accuracy). Therefore, there is neither a fermion doubling problem nor is the algorithm restricted to certain values of the flavor number N_f ; in fact, N_f can even be a continuous number.

Another advantage of the worldline numerical approach is given by the fact that chiral symmetries can manifestly be preserved. For instance in the case of the Thirring model [discussed in more detail in Appendix A], the $\text{SU}(N_f)_R \times \text{SU}(N_f)_L$ remains unaffected also in the discretized version of the worldline approach. This is because the derivation of the worldline representation is completely done in the continuum, each step preserving the chiral properties of the Dirac operator. The final worldline expression (A.5) hence is manifestly chirally invariant. Discretizing the proper-time does not spoil this invariance; moreover, spacetime remains continuous even after proper-time discretization. Even if we decided to discretize the worldline integrals by constraining them to form chains of links on a spacetime lattice, chiral symmetry would not be violated, since such a discretization would not correspond to a lattice Dirac operator. We conclude that the numerical worldline Monte Carlo estimate for the effective action respects chiral invariance, has no doubling problem and can be used for any number of flavors N_f .

2.3 Renormalization

Renormalization of these fermionic models in the large- N_f limit can be done in the standard fashion, using, e.g., Coleman-Weinberg renormalization conditions to fix physical parameters. The large- N_f limit even facilitates renormalization in any dimension D , requiring, of course, an increasing number of counter terms corresponding to physical parameters for

increasing D .¹

In practice, however, renormalization can become an issue if the computation is done numerically, since divergent pieces have to be separated from the physical quantities in a well-controlled manner. Therefore, we briefly outline the renormalization process in the following in order to demonstrate that the renormalization can be done analytically first in our formalism, such that numerics has to deal only with the remaining finite parts. For simplicity, we confine ourselves to $D = 1 + 1$ in the Gross-Neveu model but the same strategy can be applied also in the case of other fermionic models.

The unrenormalized large- N_f effective action in the Gross-Neveu model reads

$$\Gamma[\sigma] = \int d^2x \frac{N_f}{2g_\Lambda^2} \sigma^2 + \frac{N_f}{(4\pi)} \int_{1/\Lambda^2}^{\infty} \frac{dT}{T^2} \int d^2x \langle e^{-\int_0^T d\tau \sigma^2} \Phi[\sigma] - 1 \rangle_x, \quad (2.13)$$

where we have already included the free-field subtraction, such that $\Gamma[\sigma = 0] = 0$, and labeled the bare coupling with a subscript Λ . A logarithmic cutoff dependence is generated from the small- T limit of the proptime integrand. The small- T expansion of the worldline expectation value, which corresponds to the heat-kernel expansion, yields

$$\langle e^{-\int_0^T d\tau \sigma^2} \Phi[\sigma] - 1 \rangle_x = -\sigma^2(x)T + \mathcal{O}(T^2), \quad (2.14)$$

where only the term linear in T supports a $\log \Lambda$ divergence. This divergence corresponds to the local counter term proportional to the bare action and can be absorbed by a coupling renormalization. We fix the physical coupling at the renormalization scale μ by a renormalization condition of Coleman-Weinberg type:

$$\left. \frac{\delta^2 \Gamma[\sigma]}{\delta \sigma^2} \right|_{\sigma=\mu} = \frac{N_f}{g^2(\mu)}. \quad (2.15)$$

Inserting Eq. (2.13), this relates the bare to the renormalized coupling,

$$\frac{1}{g(\mu)^2} = \frac{1}{g_\Lambda^2} + \frac{1}{2\pi} \left(C + 2 + \ln \frac{\mu^2}{\Lambda^2} \right), \quad (2.16)$$

where C denotes the Euler-Mascheroni constant. Also the β function can be read off, $\beta_{g^2} \equiv \mu \partial_\mu g(\mu)^2 = -\frac{1}{\pi} g(\mu)^4$. The finite parts are specific to our proptime cutoff regularization; of course, any other desired regularization method can also be used, such that the final numerical results can be mapped to any given regularization scheme.

The renormalization scale and the coupling can be traded for an RG invariant mass scale, manifesting dimensional transmutation. A convenient choice is given by the minimum m of the effective action which is directly related to the induced fermion mass,

$$\left. \frac{\delta \Gamma}{\delta \sigma} \right|_{\sigma=m, \Lambda \rightarrow \infty} = 0 \quad \implies \quad m = \mu e^{-\frac{\pi}{g(\mu)^2} + 1}. \quad (2.17)$$

¹Beyond the large- N_f limit, the models are perturbatively renormalizable in $D = 1 + 1$. For instance in $D = 2 + 1$, they are even nonperturbatively renormalizable owing to the occurrence of a non-Gaussian fixed point, as can be proven, e.g., to all order in a $1/N_f$ expansion [52, 25].

Expressing the bare coupling in terms of the renormalized coupling and successively in terms of the minimum m , leads us to the final renormalized form of the effective action,

$$\Gamma[\sigma] = \frac{N_f}{4\pi} \int d^2x \left[-\sigma^2 + \int_0^\infty \frac{dT}{T^2} \left(\langle e^{-\int_0^T d\tau \sigma^2} \Phi[\sigma] \rangle_x - \frac{\sigma^2}{m^2} (e^{-m^2 T} - 1) - 1 \right) \right], \quad (2.18)$$

which holds for any given background $\sigma(x)$. Note that the worldline expectation value that is to be computed numerically is finite. Together with the subtraction terms, also the propertime integral is finite in the limit $\Lambda \rightarrow \infty$, which we have performed already in Eq. (2.18). For constant σ , we have $\langle e^{-\int_0^T d\tau \sigma^2} \Phi[\sigma] \rangle_x = e^{-\sigma^2 T}$, and the effective action can be calculated analytically,

$$\Gamma[\sigma = \text{const.}] = \frac{N_f}{4\pi} \int d^2x \left[\sigma^2 \left(\ln \frac{\sigma^2}{m^2} - 1 \right) \right], \quad (2.19)$$

exhibiting a nontrivial minimum at $\sigma = m$ giving rise to chiral symmetry breaking and fermion mass generation.

For the present work, the representation Eq. (2.18) is not only conceptually satisfactory, but also useful from a practical viewpoint, since the minimum m which sets the physical scale is under control analytically, cf. Eq. (2.19). For the remainder of this subsection, we briefly consider an alternative but equally valid choice of the scale.

The disadvantage of the above scale fixing lies in the fact that m is determined from the minimum of the full effective action, which happens to be at $\sigma = \text{constant}$ in the large- N_f limit. In the general case, e.g., beyond large N_f or in a fully nonperturbative calculation, the true minimum of Γ may not be known (or at least relatable to the renormalized coupling) beforehand. Still, a suitable subtraction scale is required for the computation. An alternative choice is, for instance, given by the average field $\bar{\sigma}^2 = \frac{1}{\Omega_2} \int d^2x \sigma(x)^2$, where Ω_2 is the $1 + 1$ dimensional spacetime volume. With this choice, the large- N_f renormalized effective action becomes

$$\Gamma[\sigma] = \frac{N_f}{4\pi} \int d^2x \left[\bar{\sigma}^2 \left(\ln \frac{\bar{\sigma}^2}{m^2} - 1 \right) + \int_0^\infty \frac{dT}{T^2} \left(\langle e^{-\int_0^T d\tau \sigma^2} \Phi[\sigma] \rangle_x - e^{-\bar{\sigma}^2 T} \right) \right], \quad (2.20)$$

where m is still defined via Eq. (2.17). This choice of the subtraction scale has been used in [53]. Beyond large N_f or fully nonperturbatively, the first log term will be replaced by a more complicated effective action, but the fermion loop contribution can still be computed in this manner and remains finite.

3. Spatially inhomogeneous σ condensates

3.1 Worldline formalism

A number of nontrivial tests of the preceding general worldline approach can already be performed within the Gross-Neveu model in $D = 1 + 1$ which we will exclusively consider in the following. For the case of static but spatially varying σ condensates, a number of

exact results can be derived, and these serve as stringent tests and controls of our general worldline approach. Special attention will be paid to bound states, especially zero modes and near-zero modes, as these pose the greatest numerical challenges.

For a static but spatially varying $\sigma(x)$, the renormalized action in the 1+1 dimensional Gross-Neveu model at large N_f boils down to

$$\Gamma[\sigma] = \frac{N_f}{4\pi} \int d^2x \left[-\sigma^2 + \int_0^\infty \frac{dT}{T^2} \left(\left\langle e^{-\int_0^T d\tau \sigma^2} \cosh\left(\int_0^T d\tau \sigma'\right) \right\rangle_x - \frac{\sigma^2}{m^2} (e^{-m^2 T} - 1) - 1 \right) \right], \quad (3.1)$$

where the prime denotes the derivative with respect to the spatial coordinate, $\sigma' = \partial\sigma/\partial x$. It is convenient to combine exponential and hyperbolic function in the expectation value by defining

$$V_\pm(x) := \sigma^2(x) \pm \sigma'(x) \quad , \quad (3.2)$$

and

$$\Gamma = \frac{N_f}{2} \int d^2x (\mathcal{L}_+ + \mathcal{L}_-) \quad , \quad (3.3)$$

where

$$4\pi\mathcal{L}_\pm := -V_\pm + \int_0^\infty \frac{dT}{T^2} \left(\left\langle e^{-\int d\tau V_\pm} \right\rangle_x - \frac{V_\pm}{m^2} (e^{-m^2 T} - 1) - 1 \right). \quad (3.4)$$

So far, we have not specified the details of the worldline ensemble. For a comparison with analytical results, common-point (CP) loops are particularly useful, since then we can write the associated expectation value as a quantum mechanical transition amplitude in imaginary time,

$$\left\langle e^{-\int d\tau V_\pm} \right\rangle_{x_{\text{CP}}} = \frac{\langle x | e^{-T(-\partial_1^2 + V_\pm)} | x \rangle}{\langle x | e^{-T(-\partial_1^2)} | x \rangle} = \sqrt{4\pi T} \langle x | e^{-TH_\pm} | x \rangle \equiv \sqrt{4\pi T} K_\pm(x; T) \quad . \quad (3.5)$$

Here we have introduced the Hamiltonian $H_\pm = -\partial_1^2 + V_\pm$, and the heat kernel $K_\pm(x; T)$, with $x \equiv x_{\text{CP}}$ being the common point. We have normalized the heat kernel such that it agrees with the standard conventions of 1D quantum mechanical transition amplitudes. For example, with a homogeneous condensate $\sigma(x) = m$, we have $V_\pm = m^2$, and

$$K_\pm(x; T) = \frac{e^{-m^2 T}}{\sqrt{4\pi T}} \quad . \quad (3.6)$$

The transition amplitude, or heat kernel, in turn can be written as a sum over the eigenmodes ψ_n of the Hamiltonian H_\pm :

$$K_\pm(x; T) \equiv \langle x | e^{-TH_\pm} | x \rangle = \sum_n |\psi_n(x)|^2 e^{-TE_\pm^n}, \quad (3.7)$$

where the eigenvalues of the Hamiltonian are denoted by E_\pm^n . This spectral decomposition fixes the large- T behavior of the worldline expectation value. If the Hamiltonian H_\pm has no zero mode, then all terms of the sum are exponentially damped and the expectation value vanishes for large T . By contrast, if a zero mode exists and the spectrum is discrete

at its lower end the transition amplitude Eq. (3.7) maps out the zero-mode shape $|\psi_0(x)|^2$ and the expectation value increases proportional to \sqrt{T} for large T ,

$$\left\langle e^{-\int d\tau V_{\pm}} \right\rangle \xrightarrow{T \rightarrow \infty} \sqrt{4\pi T} |\psi_0(x)|^2. \quad (3.8)$$

The case with a zero mode is numerically challenging, as is discussed in detail below.

In the following sections, we present some exact expressions for $\langle e^{-\int_0^T d\tau V_{\pm}} \rangle$ for certain inhomogeneous condensates $\sigma(x)$, and we then compare these exact expressions to the numerical worldline results. These inhomogeneous condensates are taken from known inhomogeneous solutions to the gap equation of the GN model [50, 28, 29]. This serves as a precise test and control of our numerical scheme. These exact results are derived from the corresponding exact resolvents, derived in Appendix B using the Gel'fand-Dik'ii equation (B.4, B.5), by an inverse Laplace transform:

$$R_{\pm}(x; -\lambda) \equiv \langle x | \frac{1}{H_{\pm} + \lambda} | x \rangle = \int_0^{\infty} dT e^{-\lambda T} \langle x | e^{-H_{\pm} T} | x \rangle. \quad (3.9)$$

For example, with a homogeneous condensate $\sigma(x) = m$, $V_{\pm} = m^2$, so the resolvent follows trivially from (B.4). We find $R_{\pm}(x; -\lambda) = \frac{1}{2\sqrt{m^2 + \lambda}}$, which leads to the familiar result (3.6) by an inverse Laplace transform.

3.2 Single kink condensate

Consider the inhomogeneous kink-like condensate, studied by inverse scattering in [50],

$$\sigma(x) = A \tanh(Ax). \quad (3.10)$$

The associated effective Schrödinger potentials (3.2) are

$$V_{\pm} = \begin{cases} A^2 \\ A^2(1 - 2 \operatorname{sech}^2(Ax)) \end{cases}. \quad (3.11)$$

The kink condensate $\sigma(x)$, and the corresponding $V_{\pm}(x)$, are plotted in Fig. 1. The potential $V_{-}(x)$ has an exact zero mode, localized on the kink.

The diagonal resolvents $R_{\pm}(x; -\lambda)$ are derived in Appendix B, and an inverse Laplace transform gives the corresponding exact heat kernels:

$$K_{\pm}(x; T) = \begin{cases} \frac{e^{-A^2 T}}{\sqrt{4\pi T}} \\ \frac{e^{-A^2 T}}{\sqrt{4\pi T}} + \frac{A}{2} \operatorname{Erf} \left(A\sqrt{T} \right) \operatorname{sech}^2(Ax) \end{cases}, \quad (3.12)$$

where the error function is $\operatorname{Erf}(z) = \frac{2}{\sqrt{\pi}} \int_0^z e^{-t^2} dt$. According to Eqs. (3.7), (3.8), the zero mode of the V_{-} potential is reflected in the large T behavior of $K_{-}(x; T)$: $K_{-}(x; T \rightarrow \infty) \rightarrow \frac{A}{2} \operatorname{sech}^2(Ax) \equiv |\psi_0(x)|^2$.

Capturing the zero-mode physics is indeed a precarious if not pathological problem for the standard worldline algorithm discussed above. Close to the origin, the potential V_{-} is negative, see Fig. 1, and consequently the exponent in $e^{-\int_0^T d\tau V_{-}(x(\tau))}$ is positive for certain

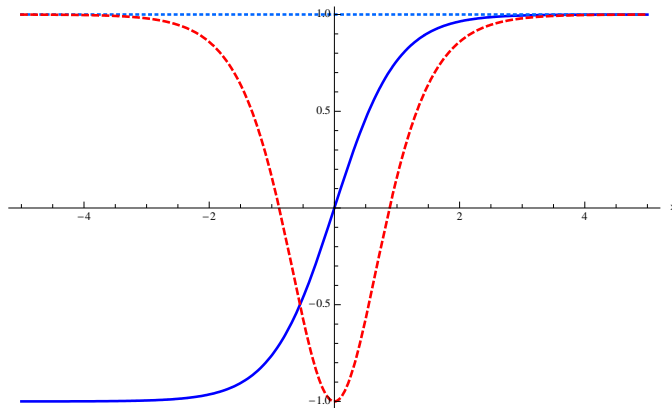


Figure 1: Plots of the kink condensate $\sigma(x)$ in Eq. (3.10) [solid, dark blue, line], and the potentials $V_{\pm}(x)$ in Eq. (3.11). The potential V_- [dashed, red, line] is localized on the kink, while V_+ [dotted, light blue, line] is constant. These plots are for $A = 1$.

loops. Comparatively small loops with many points close to the origin can exponentially dominate the expectation value for large T , inducing an overlap problem for the Monte Carlo estimate. A similar overlap problem has been studied in [47].

According to Eq. (3.8), the zero mode leads to a \sqrt{T} increase of the exact worldline expectation value. It is immediately clear that a finite and discrete loop ensemble cannot capture this property for $T \rightarrow \infty$: since the distance between two neighboring points of a discretized loop scales with \sqrt{T} , any loop ensemble will eventually no longer resolve the negative peak of V_- for large T , losing the information about the zero mode. Thus, for any finite, discrete loop ensemble generated with respect to the free worldline action, the expectation value eventually decreases exponentially in the large T limit.

In Fig. 2, the analytic result for the expectation value $\langle e^{-\int_0^T d\tau V_-(x(\tau))} \rangle$ at the origin, i.e., the center of the kink, for $A = 1$ is compared to the worldline numerical result for two loop ensembles with different numbers of loops. For small proper times, the results agree nicely. However, for large T values, the numerical results indeed decrease exponentially; the values obtained using a smaller loop ensemble decrease more rapidly than the result computed with more loops. In this large T region, the statistical errors are much smaller than the real error, which is typical for an overlap problem. Let us stress, however, that the worldline estimate is still reliable for a much larger range of proper time than the first- or second-order heat-kernel expansion, which is an asymptotic small- T expansion [see Appendix B.5] that fails for proper times larger than $\mathcal{O}(1)$. These heat-kernel expansion approximations are also plotted in Fig. 2, and we see clearly that the worldline result is far superior at large proper time T .

We conclude that the zero-mode-induced overlap problem inhibits a straightforward calculation of the heat kernel's large T behavior and can only be shifted to larger T values by using a larger loop ensemble. In Subsect. 3.6, we demonstrate that the overlap problem can be solved by generating an adapted ensemble with a Hybrid Monte Carlo algorithm.

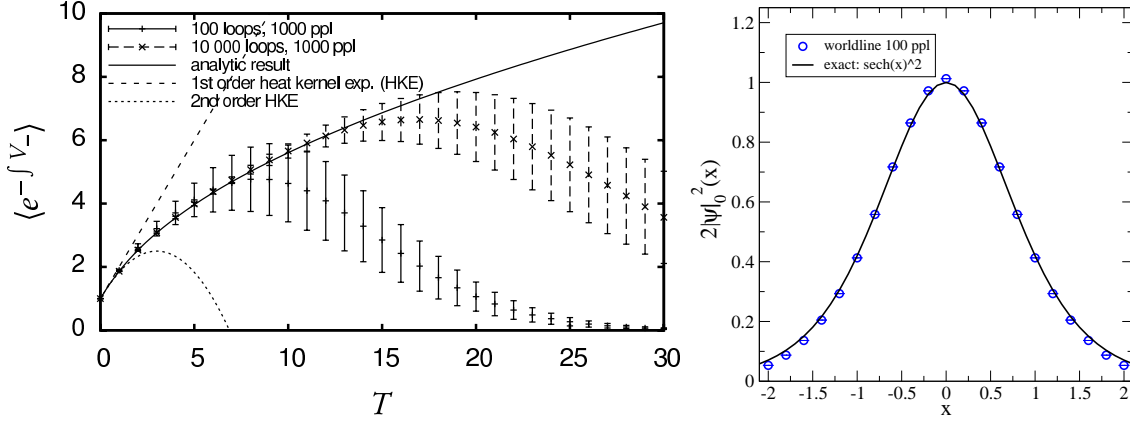


Figure 2: Left panel: the CP-loop expectation value at the centre of a kink potential with $A = 1$ versus the proper time T . For large proper times, the analytic result is proportional to \sqrt{T} . This is rediscovered by worldline numerics only up to a certain proper time value, depending on the number of loops employed. Still, the worldline estimate is reliable over a much larger range of proper times than the first- and second-order heat-kernel expansion. Right panel: zero-mode wave function of the kink with $A = 1$ reconstructed from the worldline computation of the heat kernel at large T using a CP loop ensemble.

In the present kink case, the zero-mode physics can still be identified with the standard free ensemble, since it is clearly separated from the remaining spectrum. Already at finite but large T , the heat kernel is essentially determined by the zero-mode contribution, with all other modes being exponentially suppressed. The right panel of figure 2 shows the zero-mode shape extracted from the heat kernel at a range of proper time values T of $\mathcal{O}(10)$ using 50000 CP loops consisting of 100 points per loop. In this proper time range, the modulus of the zero-mode wavefunction $|\psi_0|^2$ can be reconstructed from (3.7) by a fit. Comparison with the exact result reveals that a rather rough discretisation of the loops already yields quite accurate results.

3.3 Kink-antikink pair condensate

The single-kink condensate discussed in the previous subsection has an exact zero mode for $V_-(x)$, which complicates the worldline numerics at large T . In this section, we probe this phenomenon more precisely by considering a condensate for which the bound state is shifted away from zero energy. Consider the kink-antikink configuration:

$$\begin{aligned} \sigma(x) &= A \{ \coth(b) + [\tanh(Ax) - \tanh(Ax + b)] \} \\ &= A \{ [\coth(b) - \tanh(b)] + \tanh(b) \tanh(Ax) \tanh(Ax + b) \}. \end{aligned} \quad (3.13)$$

which has the form of a kink-antikink pair, with finite separation b/A . The corresponding potentials (3.2) are

$$V_{\pm} = A^2 \left(\coth^2(b) - 2 \left\{ \frac{\text{sech}^2(Ax + b)}{\text{sech}^2(Ax)} \right\} \right). \quad (3.14)$$

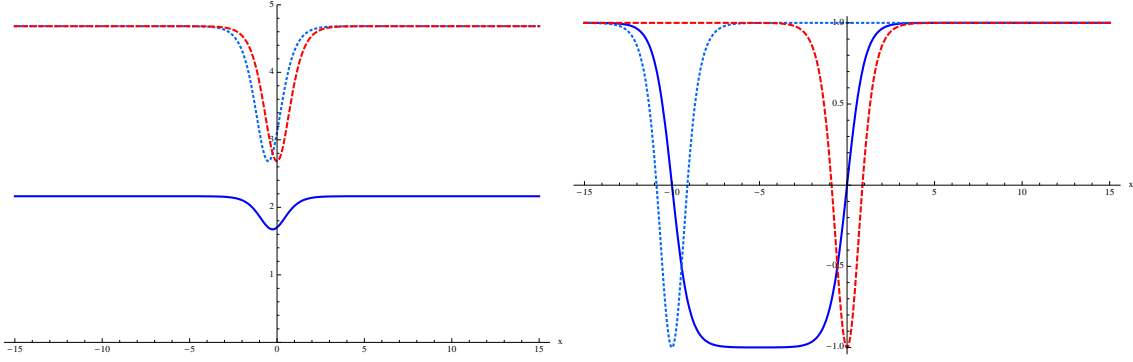


Figure 3: Plots of the kink condensate $\sigma(x)$ in Eq. (3.13) [solid, dark blue, lines], and the potentials $V_{\pm}(x)$ in Eq. (3.14). The first plot is for $b = 0.5$, while the second plot is for $b = 10$. Both plots have $A = 1$. Note that, in each case, the potential V_- [dashed, red, line] is localized on the kink, while V_+ [dotted, light blue, line] is localized on the anti-kink.

The kink-antikink condensate $\sigma(x)$, and the corresponding $V_{\pm}(x)$, are plotted in Figure 3. The potentials in Eq. (3.14) are special in the sense that they are reflectionless, and each has a *single* bound state, located at $A^2/\sinh^2(b)$, and a continuum starting at $A^2 \coth^2(b)$. Note that in the limit $b \rightarrow \infty$, the antikink disappears to minus infinity and we are left with the single kink configuration $\sigma(x) = A \tanh(Ax)$, as in Eq. (3.10). To see this pictorially, compare the second plot in Figure 3, in the vicinity of $x = 0$, with Figure 1. Correspondingly, the bound state at $A^2/\sinh^2(b)$ becomes a zero mode in this infinite separation limit.

The resolvents $R_{\pm}(x; -\lambda)$ for the potentials V_{\pm} are derived in Appendix B, and the heat kernels follow from the inverse Laplace transform (3.9):

$$K_{\pm}(x; T) = \frac{e^{-A^2 \coth^2(b) T}}{\sqrt{4\pi T}} + \frac{A}{2} e^{-A^2 T/\sinh^2(b)} \text{Erf}\left(A\sqrt{T}\right) \left\{ \begin{array}{c} \text{sech}^2(Ax + b) \\ \text{sech}^2(Ax) \end{array} \right\}. \quad (3.15)$$

For finite b , the bound state at $A^2/\sinh^2(b)$ is reflected in the exponential factor in the second term in (3.15). Thus, the large- T behaviour isolates the lowest energy mode, the bound state at energy $E_{\text{b.s.}}$:

$$K_{\pm}(x; T) \rightarrow e^{-E_{\text{b.s.}} T} |\psi_{\pm}^{\text{b.s.}}(x)|^2, \quad T \rightarrow \infty. \quad (3.16)$$

In the limit $b \rightarrow \infty$, this bound state becomes a zero mode, and the heat kernels in (3.15) reduce to those of the single-kink (3.12). In the limit $b \rightarrow 0$, $A \rightarrow 0$, with $A \coth b \equiv m$ fixed, $\sigma(x) \rightarrow m$, and $K_{\pm}(x; T)$ reduce to the heat kernels (3.6) appropriate for a homogeneous condensate. For a comparison with worldline Monte Carlo results, we only consider the challenging bound-state contribution contained, e.g., in $K_-(x; T)$ [clearly $K_+(x; T)$ yields the analogous result for \mathcal{L}_+]. This corresponds to the second term in Eq. (3.15), yielding a bound-state contribution to the action density, i.e., the Lagrangian,

$$\mathcal{L}_{-, \text{b.s.}}(x) = \frac{1}{4\pi} \frac{A}{2} \text{sech}^2(Ax) \int_0^{\infty} \frac{dT}{T} e^{-A^2 T/\sinh^2(b)} \text{Erf}(A\sqrt{T}) - \text{c.t.} \quad (3.17)$$

For illustration, we fix the parameter b by $A \coth b = 1$, so that the bound state energy is at $E_{\text{b.s.}} = 1 - A^2$. This choice minimizes the contribution of the continuum part of the spectrum to the action. Including explicit counter terms, satisfying Coleman-Weinberg renormalization conditions, we obtain (setting $m = 1$)

$$\mathcal{L}_{-, \text{b.s.}}(x) = \frac{A}{4\pi} \text{sech}^2(Ax) \int_0^\infty \frac{dT}{T^2} \left(\sqrt{\pi T} e^{-(1-A^2)T} \text{Erf}(A\sqrt{T}) + 2A(e^{-T} - 1) \right). \quad (3.18)$$

The remaining free amplitude parameter A determines the depth of the V_- potential: $A = 1$ corresponds to the single kink, with an exact zero mode, whereas $A = 0$ yields a constant, positive potential, with no bound state; intermediate values interpolate between both extremes. If A is larger than $1/\sqrt{2}$, the potential becomes negative at the origin. But only for $A = 1$, there is a zero mode and the integrand in Eq. (3.18) is proportional to \sqrt{T} in the limit $T \rightarrow \infty$.

We have performed a worldline numerical computation for five potentials with A values between $1/\sqrt{2}$ and 1, using the standard free ensemble in order to study the overlap problem quantitatively. The result corresponding to the proptime integral in Eq. (3.18) is shown in Figure 4. This analysis shows that, in general, the negative minimum of the potential is not a problem. Only for the largest A value, $A = 0.995$, for which $E_{\text{b.s.}} = 0.00099975$, does the algorithm have a severe convergence problem. In this case, the influence of the near-zero mode becomes noticeable: the exponential factor in the integrand of Eq. (3.18) decreases only weakly, and the integral is dominated by large proptime values, at which the worldline numerical evaluation of the expectation value suffers from the overlap problem, similar to that displayed in Fig. 2. Whether or not a severe overlap problem occurs can be estimated from the near-zero mode properties. A near-zero mode creates a \sqrt{T} increase of the worldline expectation value at intermediate T values, being followed by an exponential decrease at very large T values. The crossover occurs at T values $T \sim 1/E$, where E corresponds to the near-zero mode's energy level. For instance, for the above kink-antikink case with $A = 0.9995$, the crossover occurs at $T \simeq (1 - A^2)^{-1} \sim 10^3$, implying that a reliable estimate of the integrand up to values of $T \sim 10^3$ would be needed in order to solve the overlap problem by brute force. For the case with $A = 0.942809$, the crossover occurs already at $T \simeq (1 - A^2)^{-1} \sim 9$ which is well resolvable by the standard algorithm with 1000 loops or more, cf. Fig. 2.

3.4 Periodic array of kink-antikink pairs

Next, consider a crystalline condensate formed from a periodic array of kink-antikink pairs:

$$\begin{aligned} \sigma(x) &= A \left(\left[Z(b; \nu) + \frac{\text{cn}(b; \nu) \text{dn}(b; \nu)}{\text{sn}(b; \nu)} \right] + [Z(Ax; \nu) - Z(Ax + b; \nu)] \right) \\ &= A \left(\frac{\text{cn}(b; \nu) \text{dn}(b; \nu)}{\text{sn}(b; \nu)} + \nu \text{sn}(b; \nu) \text{sn}(Ax; \nu) \text{sn}(Ax + b; \nu) \right). \end{aligned} \quad (3.19)$$

Here $Z(x; \nu)$ is the Jacobi zeta function, and sn , cn and dn the Jacobi elliptic functions, all with real elliptic parameter $0 \leq \nu \leq 1$ [54, 55]. This type of inhomogeneous condensate

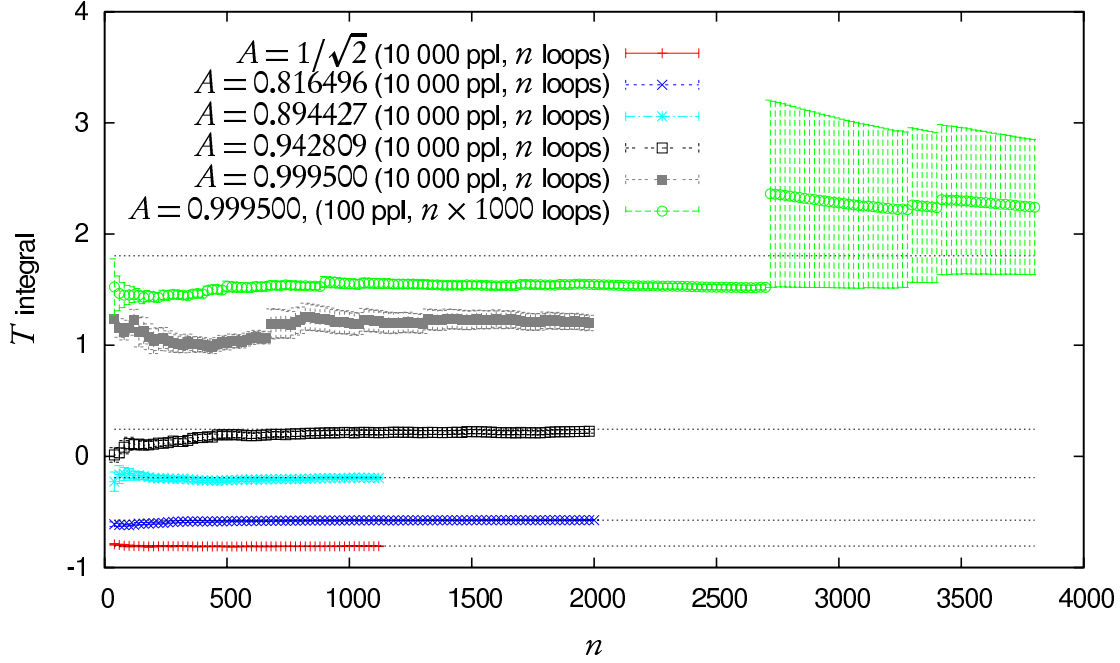


Figure 4: Convergence behaviour of the worldline-numerical result for near-zero mode contributions. The plot shows the numerical values corresponding to the proper-time integral Eq. (3.18) versus the number of loops employed for different A values. The topmost values (green circles) are for the same A value as the values immediately below (solid grey squares), but with the number of loops multiplied by a factor of 1000. The dotted horizontal lines represent the analytic values. The error bars are the jackknife estimates and should provide reasonable values if the number of loops is larger than 1000. Evidently, this is not the case for the largest A value. This indicates an overlap problem. At about 2 750 000 loops ($n = 2750$), we observe a huge jump of the result, apparently caused by the occurrence of one single very small loop.

is physically important in a number of contexts: it represents a bipolaron crystal in conducting polymers [56], and it characterizes a crystalline phase in the massive GN model [28]. In the limit $\nu \rightarrow 1$ we recover the kink-antikink configuration (3.13), since in this limit: $\text{sn}(b; \nu) \rightarrow \tanh(b)$, $Z(b; \nu) \rightarrow \tanh(b)$, $\text{cn}(b; \nu) \rightarrow \text{sech}(b)$, and $\text{dn}(b; \nu) \rightarrow \text{sech}(b)$. Note that we can restrict to $0 \leq b \leq \mathbf{K}(\nu)$, because of the periodicity of the Jacobi elliptic functions. When $b = \mathbf{K}(\nu)$, this condensate is important for soliton lattices in polymers [56, 57], for the Peierls model [58], for periodic phases in superconductors [59], and for the crystal phase of the massless GN model [28]. In this case, discussed in more detail in the next subsection, the neighbouring antikinks lie at the very edge of the period, and so in the infinite period limit [$\nu \rightarrow 1$], the antikinks disappear to plus/minus infinity, and we are left with the single-kink configuration (3.10). Thus, the configuration (3.19) contains all the other examples as special cases in a particular parametric limit.

The potentials (3.2) corresponding to the periodic condensate (3.19) are

$$V_{\pm} = A^2 \left(\frac{1}{\text{sn}^2(b; \nu)} - 1 + \nu - 2\nu \left\{ \frac{\text{cn}^2(Ax + b; \nu)}{\text{cn}^2(Ax; \nu)} \right\} \right). \quad (3.20)$$

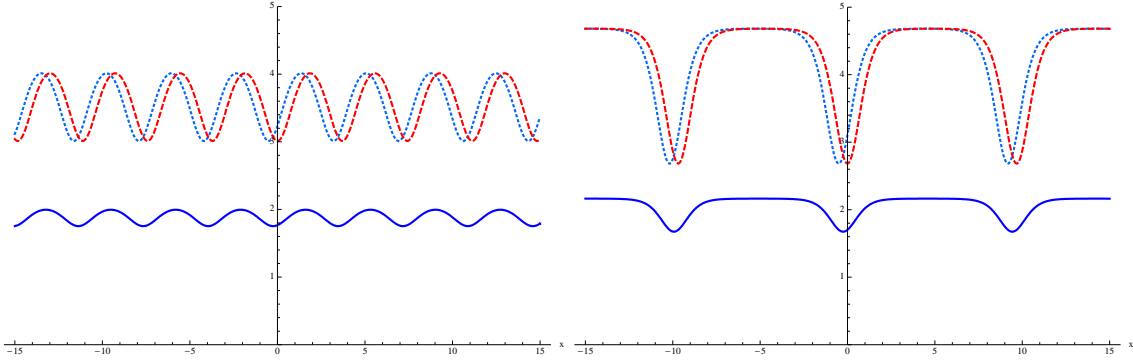


Figure 5: Plots of the periodic condensate $\sigma(x)$ in Eq. (3.19) and of the periodic potentials $V_{\pm}(x)$ in Eq. (3.20). The first plot is for elliptic parameter $\nu = 0.5$, for which $\mathbf{K}(0.5) = 1.85$, while the second plot is for $\nu = 0.999$, for which $\mathbf{K}(0.999) = 4.84$. In each plot, $A = 1$ and $b = 0.5$. The solid [dark blue] curves are the periodic condensates. Note that $V_{-}(x)$ [dashed, red, lines] are localized on the kink, while $V_{+}(x)$ [dotted, light blue, lines] are localized on the antikink. Notice that as $\nu \rightarrow 1$, the period diverges, and we recover the kink-antikink configuration: compare the second plot with the first plot in Figure 3.

The kink-antikink crystal condensate $\sigma(x)$, and the corresponding $V_{\pm}(x)$, are plotted in Figure 5.

These potentials are periodic functions, with period $2\mathbf{K}(\nu)/A$, and are special in the sense that they possess only a *single* bound band – they are the simplest example of the “finite-gap” potentials [60], which are the periodic analogue of reflectionless potentials. $V_{\pm}(x)$ are the same function, displaced in x , and so they have precisely the same band spectrum. In the language of supersymmetric quantum mechanics, they are self-isospectral [61]. The band spectrum is plotted in Figure 6. The band edges lie at $A^2 \text{cs}^2(b; \nu)$ and $A^2 \text{ds}^2(b; \nu)$, and with a continuum starting at $A^2 \text{ns}^2(b; \nu)$. As $\nu \rightarrow 1$, the period diverges, and the bound band shrinks to a single bound state at $A^2/\sinh^2(b)$, which is just the bound state of the reflectionless system associated with the single kink-antikink pair.

The resolvents for the potentials in (3.20) are derived in Appendix B, and the corresponding propagators are obtained by an inverse Laplace transform:

$$K_{\pm}(x; T) = \alpha(T) + \beta(T) \begin{Bmatrix} \text{cn}^2(Ax + b; \nu) \\ \text{cn}^2(Ax; \nu) \end{Bmatrix} . \quad (3.21)$$

Note that the coefficients $\alpha(T)$ and $\beta(T)$ are the same for the two propagators – the only difference between K_{+} and K_{-} is the shift of the x dependence in the cn^2 functions. The coefficients are most usefully expressed in the convolution form:

$$\beta(T) = \frac{\nu A^2}{2} e^{-A^2 \text{ds}^2(b; \nu) T} \int_0^T du \frac{e^{-A^2(\nu-1/2)u}}{\sqrt{\pi(T-u)}} I_0\left(\frac{A^2}{2}u\right) \quad (3.22)$$

$$\alpha(T) = \frac{1}{\nu} \left(\text{ds}^2(b; \nu) \beta(T) + \frac{1}{A^2} \frac{d\beta}{dT} \right) . \quad (3.23)$$

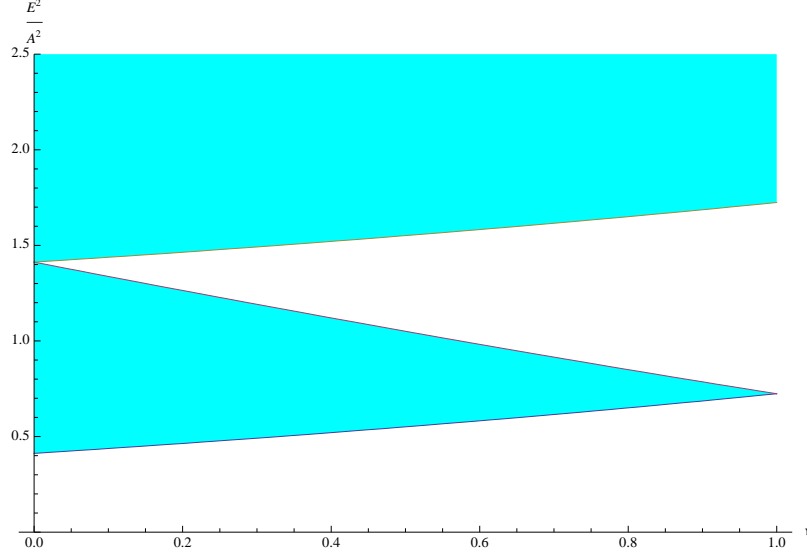


Figure 6: The spectrum of the Schrödinger operators H_{\pm} with $\sigma(x)$ given by the periodic condensate Eq. (3.19), as a function of the elliptic parameter ν . The spectrum has a single bound band, with band edges $A^2 \text{cs}^2(b; \nu)$ and $A^2 \text{ds}^2(b; \nu)$, and a continuum band starting at $A^2 \text{ns}^2(b; \nu)$. When $\nu \rightarrow 1$, the bound band contracts to a single bound level at $A^2 / \sinh^2 b$, with the continuum edge at $A^2 \coth^2 b$. In the other limit, as $\nu \rightarrow 0$, the spectrum is pure continuum, with lower edge at $A^2 \cot^2 b$. This plot is for $b = 1$. These features can be clearly seen in the associated resolvents in the text.

When $\nu = 1$ we recover the propagators for the kink-antikink pair configuration in (3.15), while when $\nu = 0$ we find propagators for a homogeneous condensate of mass $A \cot(b)$.

An interesting special value of ν is the lemniscate case, $\nu = \frac{1}{2}$, for which $\beta(T)$ takes the simple Bessel function form

$$\beta(T) = \frac{1}{4} e^{-A^2 \text{ds}^2(b; \frac{1}{2}) T} \sqrt{\frac{\pi A^2 T}{2}} I_{\frac{1}{4}} \left(\frac{A^2 T}{4} \right) I_{-\frac{1}{4}} \left(\frac{A^2 T}{4} \right) \quad . \quad (3.24)$$

For a comparison with worldline numerics, we choose typical potential parameters as they occur in the phase diagram of the GN model at finite densities and temperature: $b = 1$, $\nu = 0.9$, and $A = m / \coth(1)$. Since this typical form of the potential is free of (near-)zero modes, it represents a direct test of the quantitative reliability of worldline Monte Carlo for fermionic fluctuations in generic backgrounds. Figure 7 shows the expectation value $\langle \exp(-\int V_-) \rangle$ versus the proptime in a minimum of the potential V_- . Due to the absence of a zero mode, the values decrease exponentially already for small proptimes, in contrast to the corresponding single kink result in Figure 2, and we see in Figure 7 that the numerical and analytic results agree very well. Even a small loop ensemble, of just 2000 loops, yields tiny errors. By contrast, the first- and second-order heat-kernel expansion, which is a standard analytic expansion technique, fails badly for $T \gtrsim 1$. For further quantitative comparison, we integrate the resulting Lagrangian \mathcal{L}_- over one period

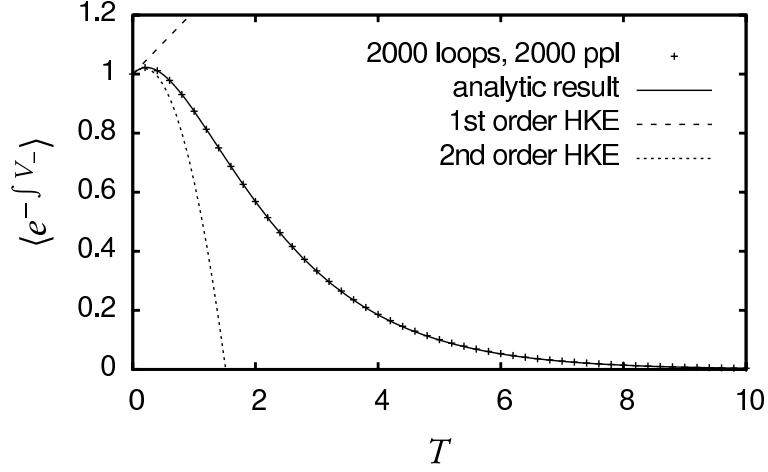


Figure 7: The worldline expectation-value versus the proper-time in a minimum of the potential V_- for $b = 1$, $\nu = 0.9$, and $A = m/\coth(1)$. The statistical error is too tiny to be plotted. Due to the absence of a zero mode, the values decrease exponentially very early, in contrast to the corresponding values for a single kink, as shown in Fig. 2. The figure above shows that the analytic heat-kernel expansion [the dashed and dotted lines] is not reliable for $T \gtrsim 1$.

along the x axis:

$$\int_0^{2K(0.9)/A} dx \mathcal{L}_- = -\frac{A}{4\pi} \begin{cases} 6.81704 & \text{(analytic)} \\ 6.818 \pm 0.001 & \text{(worldline numerics)} \end{cases} \quad (3.25)$$

where the upper value in braces is the analytic result, the lower one a worldline-numerical estimate with 20 000 CM loops of 2000 ppl each. (The result obtained for the integrated \mathcal{L}_+ is identical.) In units of m , the spatial average of \mathcal{L}_- then is

$$\begin{aligned} \overline{\mathcal{L}_-} &:= \frac{\kappa}{2K(0.9)} \int_0^{2K(0.9)/\kappa} dx \mathcal{L}_- \\ &= -\frac{m^2}{4\pi} \begin{cases} 0.766857 & \text{(analytic)} \\ 0.7669 \pm 0.0001 & \text{(worldline numerics)} \end{cases} \end{aligned} \quad (3.26)$$

Note that this is well above the corresponding value of the constant-field solution, $-1/(4\pi)$, indicating that the constant field is the preferred vacuum solution. We conclude that a precision on the permille level or below is straightforwardly achievable with worldline Monte Carlo algorithms for fermionic systems in absence of (near-)zero modes.

With the same loop ensemble we study the slightly more challenging configuration $b = 2$, $\nu = 0.9$ and $m = A \coth(2)$, which has deeper minima, and obtain

$$\int_0^{2K(0.9)} dx \mathcal{L}_- = -\frac{A}{4\pi} \begin{cases} 0.499945 & \text{(analytic)} \\ 0.49 \pm 0.03 & \text{(worldline numerics)} \end{cases} \quad (3.27)$$

with the spatial average (in units of m)

$$\overline{\mathcal{L}_-} = -\frac{m^2}{4\pi} \begin{cases} 0.0901099 & \text{(analytic)} \\ 0.088 \pm 0.005 & \text{(worldline numerics)} \end{cases} \quad (3.28)$$

The statistical error is larger, as one might have expected, but can be improved using a larger worldline ensemble. The agreement with the analytic result is still very satisfactory.

3.5 Kink crystal condensate

An important special case corresponds to choosing the kink-antikink separation to coincide with half the period of the crystal, in which case the antikinks neighboring a given kink lie at the edges of the period. This corresponds to choosing $b = K(\nu)$. Then the condensate in Eq. (3.19) simplifies to

$$\sigma(x) = A\nu \frac{\text{sn}(Ax; \nu) \text{cn}(Ax; \nu)}{\text{dn}(Ax; \nu)}. \quad (3.29)$$

The associated Schrödinger potentials are

$$V_{\pm} = A^2 \left(\nu - 2\nu \left\{ \frac{(1 - \nu) \text{sd}^2(Ax; \nu)}{\text{cn}^2(Ax; \nu)} \right\} \right). \quad (3.30)$$

The condensate and associated potentials are plotted in Figure 8.

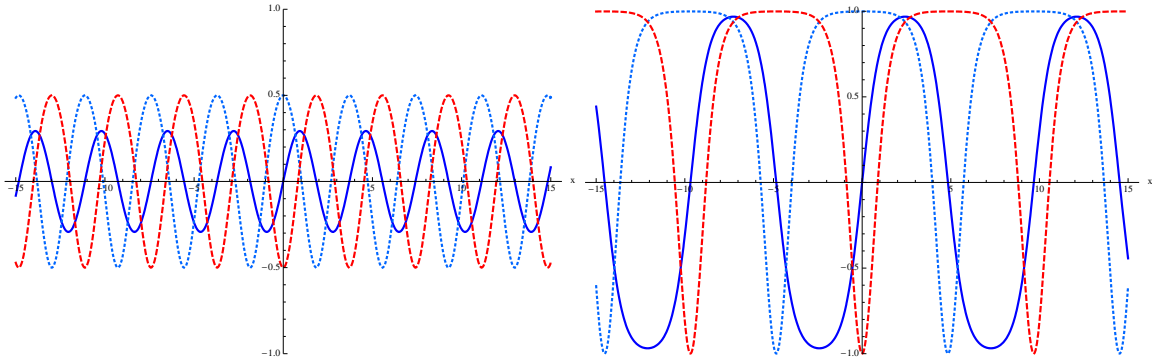


Figure 8: Plots of the periodic condensate $\sigma(x)$ [solid, dark blue, lines] in Eq. (3.29), and the periodic potentials $V_{\pm}(x)$ in Eq. (3.30), with elliptic parameter $\nu = 0.5$ [first plot] and $\nu = 0.999$ [second plot]. Both plots are for $A = 1$. Note that the antikinks lie at the edge of the period, so that $V_-(x)$ [dashed, red, line] is localized on the kinks at the center of a period, while $V_+(x)$ [dotted, light blue, line] is localized on the antikinks at the edge of a given period.

This system has a band spectrum with band edges at 0 , $A^2(1 - \nu)$, and A^2 , as shown in Figure 9. Note that the bottom of the lowest band is at 0 , for all ν , and that there is just one bound band. The corresponding heat kernels $K_{\pm}(x; T)$ can be obtained from those in the previous section by the simple substitution $b \rightarrow K(\nu)$.

3.6 Worldline ensembles from Hybrid Monte Carlo

Since the standard worldline ensembles generated with respect to the free worldline action can lead to an overlap problem for the special case of a (near-)zero mode in the fermion spectrum, let us explore a different route: we generate the ensemble with respect to the *full*

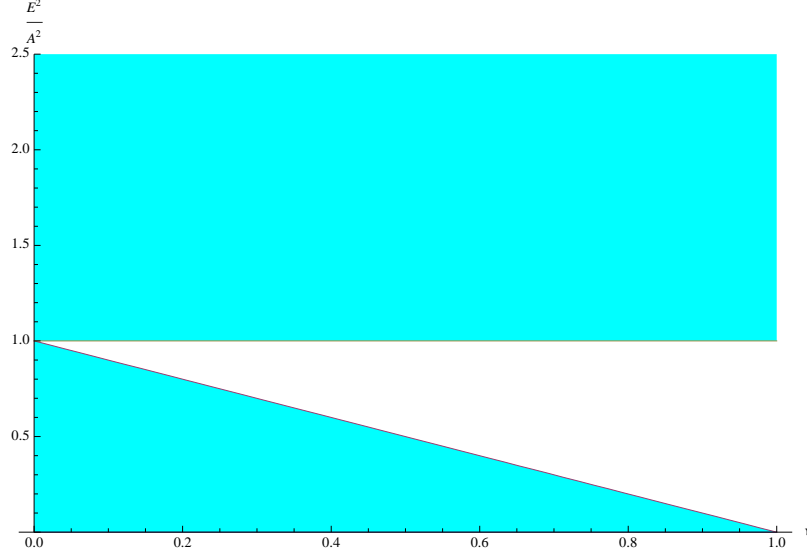


Figure 9: The spectrum of the Schrödinger operators H_{\pm} with $\sigma(x)$ given by the periodic condensate Eq. (3.29), as a function of the elliptic parameter ν . The spectrum has a single bound band, with band edges 0 and $A^2(1 - \nu)$, and a continuum band starting at A^2 . When $\nu \rightarrow 1$, the bound band contracts to a single bound level at 0. In the other limit, as $\nu \rightarrow 0$, the spectrum is pure continuum, with lower edge at 0.

action using a Hybrid Monte Carlo (HMC) algorithm. In principle, worldline generation with the full action would also be possible with a local update algorithm such as the Metropolis update. However, due to the fact that the worldlines are one-dimensional, local updates suffer from a long auto-correlation time, as observed in [43]. This is avoided by the global HMC update.

The quantity which will be central for the HMC simulation is given by

$$W(x, T) = -\frac{d}{dT} \ln K_{\pm}(x, T) = \frac{\langle x | (-\partial_1^2 + V_{\pm}) e^{-T(-\partial_1^2 + V_{\pm})} | x \rangle}{\langle x | e^{-T(-\partial_1^2 + V_{\pm})} | x \rangle}, \quad (3.31)$$

$$K_{\pm}(x, T) = \langle x | e^{-T(-\partial_1^2 + V_{\pm})} | x \rangle. \quad (3.32)$$

This quantity is given by means of an expectation value with respect to the full loop ensemble:

$$W(x, T) = \left\langle -\partial_1^2 + V_{\pm} \right\rangle_{x_F}, \quad (3.33)$$

where the loops are generated with the probability

$$P_F[x] = \delta \left(x_{\text{CM}} - \int_0^T d\tau x(\tau) \right) \exp \left[-\frac{1}{4} \int_0^T d\tau \dot{x}^2(\tau) - \int_0^T d\tau V_{\pm}(x(\tau)) \right]. \quad (3.34)$$

The strategy is to generate statistically important loop configurations $\{x(\tau)\}$ using HMC methods and to estimate $W(T, x)$ in (3.33). The advantage of this approach is that the loop ensemble already incorporates features of the potentials V_{\pm} , and that far fewer configurations are required for a reliable estimate of expectation values than for free loop clouds.

The disadvantage is that more computational resources are necessary to generate the HMC loop ensembles. Ultimately, it will depend on the particular potential whether the additional numerical effort is justified. We will argue that this is the case for a Hamiltonian $H_{\pm} = (-\partial_1^2 + V_{\pm})$ which possesses zero modes.

Once a numerical estimate for $W(x, T)$ is obtained, the heat kernel K_{\pm} can be reconstructed by integration of (3.31) with respect to the proptime. Note that the kernel satisfies the boundary condition $K_{\pm}(x, 0) = 1$. We therefore find:

$$K_{\pm}(x, T) = \exp \left\{ - \int_0^T d\tau W(x, \tau) \right\}. \quad (3.35)$$

Let us briefly comment on the implementation of the discretized loops. As before, the proptime interval $\tau = [0, T]$ is represented using N points:

$$\tau = n d\tau, \quad d\tau = \frac{T}{N}, \quad n = 1 \dots N, \quad N \text{ odd}. \quad (3.36)$$

For a simplification of the notation, we will assume that N is odd. We base the HMC algorithm on a discrete Fourier representation of the worldlines, which can easily account for the worldline periodicity and leads to uncoupled degrees of freedom for $V_{\pm} = 0$. Hence, considering the Fourier coefficients as degrees of freedom implies that loop ensembles can be generated with little autocorrelation as long as the influence of the potential is not too significant.² For CM loops, we have the representation:

$$x(\tau) = x_{\text{CM}} + \frac{\sqrt{T}}{N} \sum_{k=-\frac{N-1}{2}}^{\frac{N-1}{2}} c_k \exp \left(i \frac{2\pi}{T} k \tau \right), \quad c_{-k} = c_k^*, \quad c_0 = 0. \quad (3.37)$$

In the case of CP loops, for which x_{CP} is the common point, we analogously find

$$x(\tau) = x_{\text{CP}} + \frac{\sqrt{T}}{N} \sum_{k=-\frac{N-1}{2}}^{\frac{N-1}{2}} c_k \left[\exp \left(i \frac{2\pi}{T} k \tau \right) - 1 \right]. \quad (3.38)$$

With these representations, the worldline kinetic term is Gaußian in the weights c_k :

$$\frac{1}{4} \int_0^T d\tau \dot{x}^2(\tau) \rightarrow \frac{1}{4} \sum_{n=1}^N \frac{(x(\tau + d\tau) - x(\tau))^2}{d\tau} = \sum_k c_k c_{-k} \sin^2 \left(\frac{\pi}{N} k \right).$$

The task is now to generate statistical ensembles of the degrees of freedom

$$c_k, \quad k = -\frac{N-1}{2}, \dots, -1, 1, \dots, \frac{N-1}{2},$$

which are distributed according to, e.g., the CM probability distribution (3.34). Note that the δ -function constraint has been exactly incorporated leaving us with $2 \frac{N-1}{2} = N-1$

²An HMC algorithm could equally be based on the *v loop* algorithm [43], since it features the same necessary properties. By contrast, an HMC generalization of the *d loop* algorithm [51] which is based on an iterative loop construction seems not to be straightforward.

degrees of freedom, parameterized by the coefficients c_k . For the HMC approach, it is highly advisable to introduce real valued degrees of freedom. We therefore define the coefficients $d_k \in \mathbb{R}$ by

$$d_k = c_k + c_{-k} , \quad d_{-k} = i(c_k - c_{-k}) , \quad k = 1 \dots \frac{N-1}{2} . \quad (3.39)$$

With this definition the loop coordinates, for instance, for the CM loops (3.37) are manifestly real valued:

$$x(\tau) = x_{\text{CM}} + \frac{\sqrt{T}}{N} \sum_{k=1}^{\frac{N-1}{2}} \left\{ d_k \cos\left(\frac{2\pi}{T} k \tau\right) + d_{-k} \sin\left(\frac{2\pi}{T} k \tau\right) \right\} . \quad (3.40)$$

The next step is to introduce the canonical momentum $\pi_k \in \mathbb{R}$ for each degree of freedom d_k . The corresponding HMC Hamiltonian is defined by

$$\mathcal{H}(\pi_k, d_k) = \frac{1}{2} \sum_k [\pi_k^2 + \mathcal{V}(d_k)] , \quad (3.41)$$

$$\mathcal{V}(d_k) = \frac{1}{4} \int_0^T d\tau \dot{x}^2(\tau) + \int_0^T d\tau V_{\pm}(x(\tau)) . \quad (3.42)$$

The degrees of freedom experience an evolution with the so-called HMC time u . This time evolution is determined by the Hamilton equations of motion:

$$\frac{d}{du} d_k = \pi_k , \quad \frac{d}{du} \pi_k = - \frac{\partial \mathcal{V}(d_k)}{\partial d_k} . \quad (3.43)$$

The important property of any solution $d_k(u)$, $\pi_k(u)$ is that the HMC energy is conserved:

$$\frac{d}{du} \mathcal{H}(\pi_k(u), d_k(u)) = 0 .$$

The initial momenta $\pi_k(u=0)$ are selected at random from a Gaussian distribution. The initial coordinates $c_k(u=0)$ are given by their actual ensemble values. With these initial conditions, the values at $u = u_f$ are *approximately* obtained with the help of a Leapfrog integration of the equations of motion (3.43). Because the equations of motion are not solved exactly, the HMC energy \mathcal{H} is not exactly conserved. The idea central to the HMC approach is to accept the values $d_k(u_f)$ as new members of the Markov chain with the probability

$$p = \min\left(1, \exp\{-\Delta H\}\right), \quad \Delta H = \mathcal{H}[\pi_k(u_f), d_k(u_f)] - \mathcal{H}[\pi_k(0), d_k(0)] . \quad (3.44)$$

Since the equations of motion are satisfied to a good extent due to the Leapfrog integration, the value $c_k(u_f)$ can be largely different from $c_k(0)$ (implying good ergodicity) while the acceptance rate is still high.

In order to test the HMC approach, we revisit the kink background field (3.10) (with $A = 1$ in the following). The HMC final time is given by $u_f = N_{\text{tra}} du$ where N_{tra} is the number of steps of the Leapfrog integration. The step size du is chosen to obtain an

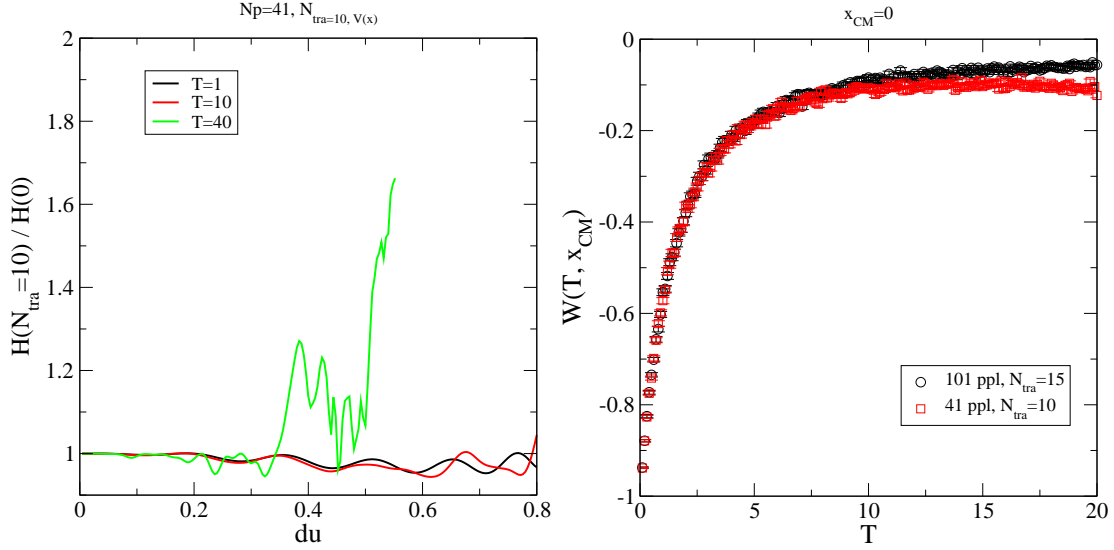


Figure 10: Left panel: the HMC energy as a function of step size du of the Leapfrog integration. Right panel: the function $W(x=0, T)$ for the kink configuration obtained with HMC loops. The large- T behavior is dominated by the ground-state energy, cf. Eq. (3.45). Sufficiently many points per loop N are required in order to observe the approach to the zero-energy mode of the kink.

acceptance rate between 20% and 80%. Figure 10 (left panel) shows the HMC energy as function of the step size du for several values for the proper time. We find that a value $du \approx 0.3$ provides a good compromise between ergodicity and acceptance rate. Using the HMC ensembles for CM loops, the function $W(x, T)$ is estimated and the heat kernel is reconstructed with the help of the proper time integration (see Eq. (3.35)). Note that because of (3.31), we find for large values of T

$$W(x, T) \approx E_0 + (E_1 - E_0) \frac{|\langle x|1\rangle|^2}{|\langle x|0\rangle|^2} e^{-(E_1 - E_0)T} \quad (T \text{ large}), \quad (3.45)$$

where E_0 , E_1 are the energies of ground and first excited states, and $|0\rangle$ and $|1\rangle$ are the corresponding wave functions. In theories with a gap between the first excited and the ground state, the latter equation implies that $W(x, T)$ rapidly approaches a constant, i.e., the ground state energy E_0 , for large T . In the worst case scenario of a zero mode, $W(x, T)$ approaches zero and a positive constant otherwise. Figure 10 (right panel) shows the result for $W(x=0, T)$ for the kink configuration. Indeed, the function $W(x, T)$ rapidly approaches a constant for large T . The overlap problem, discussed in the previous subsections, has been solved by the use of HMC loop ensembles. Note, however, that, also in the present case, the number of points per loop N must be large enough: for coarse loops, the numerical estimate approaches a negative constant thus erroneously suggesting a negative ground state energy and an instability of the operator. A sufficiently fine representation or an improved integration over loop coordinates might resolve this problem.

Finally, we present our final result for the reconstructed heat kernel in Fig. 11. We obtain very good results with HMC using only a modest number of points per loop.

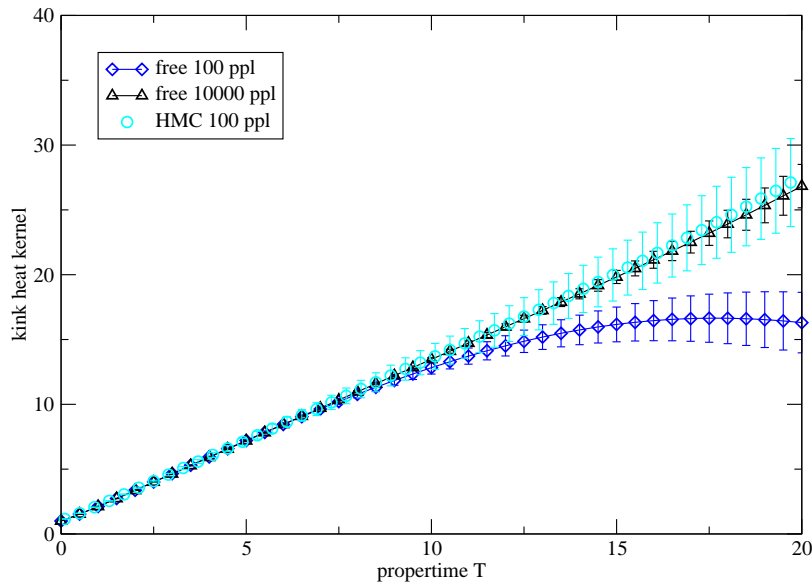


Figure 11: HMC results for the heat kernel for the kink configuration in comparison with the result obtained from free loop ensembles (all used ensembles are CM loops). Significantly fewer HMC loops are required for a reliable estimate of the large-proptime behavior.

To conclude this subsection, the overlap problem of the free loop cloud method is indeed solved by adopting the HMC approach. Note, however, that a precise estimate of the effective action in the case of a (near-)zero mode is still a numerical challenge.

4. Worldline approach at finite temperature and chemical potential

Even though introducing finite temperature and chemical potential appears straightforward in the worldline approach, special attention has to be paid to combining this straightforward formalism with Monte Carlo algorithms. The reason is that an analysis of field theories at finite temperatures and densities often requires knowledge about the analytic structure of propagators etc. in the complex energy-momentum plane, or similar conjugate variables such as the proper time. By contrast, Monte Carlo algorithms require a positive real action for importance sampling, and this restricts the computable information to lie on the real axis of given variables.

Since this conflict of interests between thermal field theory at finite density and Monte Carlo algorithms is general and not only restricted to the Gross-Neveu model, we discuss this problem in more detail in the following.

4.1 Temperature in the worldline representation

Consider the worldline formulation of a general quantum-field theoretic amplitude. Finite temperature can easily be implemented with the aid of the Matsubara formalism: The Euclidean time, say along the D th direction, is compactified to the interval $[0, \beta]$ with periodic boundary conditions for worldline fluctuations for bosonic fields and antiperiodic

boundary conditions for fermionic degrees of freedom. Here $\beta = 1/\mathcal{T}$ is the inverse temperature. (Note that we reserve the symbol T for proptime, whereas the temperature is denoted by \mathcal{T} .) As a consequence, the worldlines can also wind around the time dimension. It is convenient to write a given loop $x(\tau)$ with winding number n as sum of a loop with no winding, $\tilde{x}(\tau)$, and a translation in time running from zero to $n\beta$ with constant speed,

$$x_\mu(\tau) = \tilde{x}_\mu(\tau) + n\beta \frac{\tau}{T} \delta_{\mu D}. \quad (4.1)$$

The path integral over the different winding number sectors labeled by n factorizes for static configurations, yielding

$$\int_{x(0)=x(T)} \mathcal{D}x e^{-\int_0^T d\tau \frac{\dot{x}^2}{4}} \dots = \sum_{n=-\infty}^{\infty} (-1)^n e^{-\frac{n^2 \beta^2}{4T}} \int_{\tilde{x}(0)=\tilde{x}(T)} \mathcal{D}\tilde{x} e^{-\int_0^T d\tau \frac{\dot{\tilde{x}}^2}{4}} \dots \quad (4.2)$$

where the factor $(-1)^n$ implements antiperiodic boundary conditions for the present fermion fluctuations; it would be absent for bosons here and in the following. A finite-temperature generalization of a vacuum proptime expression is straightforwardly obtained from a simple insertion into the proptime integral,

$$\int_0^\infty dT \dots \rightarrow \int_0^\infty dT \left(\sum_{n=-\infty}^{\infty} (-1)^n e^{-\frac{n^2 \beta^2}{4T}} \right) \dots \quad (4.3)$$

where the ellipsis represent, for instance, a heat-kernel expression or a worldline expectation value etc. The winding number sum over n is directly related to the Matsubara sum by a Poisson transformation. Quantum and thermal fluctuations are separated by the different winding number sectors: the $n = 0$ term is identical to the vacuum expression, while the $|n| \geq 1$ sectors are purely thermal contributions which vanish in the vacuum limit $\beta \rightarrow \infty$.

Let us stress that the present thermal formalism not only holds in general but is also completely robust when combined with worldline Monte Carlo techniques, as has been used in the context of the Casimir effect at finite temperature [62]. The winding number sum converges rapidly in the relevant low- and intermediate temperature range; at high temperatures where increasingly more winding sectors would have to be resummed, a Poisson resummation to Matsubara sums can be performed, such that rapid convergence is guaranteed for all temperatures. In particular, analytical or numerical knowledge of the heat kernel on the real T axis is sufficient for a reliable estimate of thermodynamic amplitudes. For example, it is straightforward to derive the critical temperature for symmetry restoration in the Gross-Neveu model within the present formalism, yielding the well-known result

$$\beta_c = \pi e^{-C} m^{-1} \approx 1.76387 m^{-1}, \quad \mathcal{T}_c = 1/\beta_c \approx 0.566932 m \quad (4.4)$$

in units of m [63]. For temperatures larger than the critical temperature \mathcal{T}_c , the potential σ vanishes and the spontaneously broken discrete chiral symmetry is restored.

4.2 Chemical potential in the worldline representation

Introducing a finite chemical potential via the grand-canonical partition function leads us to the microscopic action of the Gross-Neveu model at finite density,

$$S = \int d^D x \left(-\bar{\psi} (\not{\partial} + \mu \gamma_D) \psi + \frac{g^2}{2N_f} (\bar{\psi} \psi)^2 \right), \quad (4.5)$$

in D dimensions. The resulting contribution to the effective action from fermionic fluctuations reads analogously to Eq. (2.5)

$$\Delta\Gamma[\sigma] = -\frac{N_f}{2} \text{Tr} \ln(-\bar{\partial}^2 - (\partial_D + \mu)^2 + \sigma^2 - i\not{\partial}\sigma). \quad (4.6)$$

Since the chemical potential occurs in the form of the D th component of an imaginary Euclidean gauge potential in the effective action, it is tempting to jump directly to the corresponding worldline representation in the presence of gauge fields, which are coupled to the worldline in the form of a Wegner-Wilson loop. In other words, the free worldline action receives a further contribution of the form

$$e^{-\frac{1}{4} \int_0^T d\tau \dot{x}^2} \rightarrow e^{-\frac{1}{4} \int_0^T d\tau \dot{x}^2 - \mu \int_0^T d\tau \dot{x}_D} \rightarrow (-1)^n e^{-\frac{n^2 \beta^2}{4T}} e^{-\frac{1}{4} \int_0^T d\tau \ddot{x}^2 - \mu \beta n}, \quad (4.7)$$

where in the last step we have used the decomposition of worldlines into different winding number sectors n on the finite-temperature cylinder. Since also negative winding numbers are allowed, it is already apparent that the winding number sum may suffer from convergence problems at large $\beta\mu$. This issue will be discussed in detail in the next subsection; let us simply state here that convergence problems are absent for $\beta\mu < \pi$ which we will assume in the following.

Decomposing the winding number sum into the vacuum sector $n = 0$, and the temperature and density corrections $|n| \geq 1$, implying a decomposition of the effective action (or grand potential) into a vacuum part Γ , and a thermal part $\Delta\Gamma_{\beta,\mu}$:

$$\Gamma_{\beta,\mu} = \Gamma + \Delta\Gamma_{\beta,\mu}, \quad (4.8)$$

with Γ given by Eq. (2.18), we end up with the worldline representation for the thermal contribution at finite density

$$\Delta\Gamma_{\beta,\mu} = \int d^D x \frac{N_f d\gamma}{(4\pi)^{D/2}} \int_0^\infty \frac{dT}{T^{1+D/2}} \left(\sum_{n=1}^\infty (-1)^n e^{-\frac{\beta^2 n^2}{4T}} \cosh(\mu \beta n) \right) \left\langle e^{-\int_0^T d\tau \sigma^2} \Phi[\sigma] \right\rangle. \quad (4.9)$$

For $\beta\mu < \pi$, this representation is reasonably converging and can numerically be implemented rather straightforwardly. Naively interchanging summation and integration yields rapidly converging proper-time integrals for any given n ; however, the n sum, which is reminiscent of a fugacity expansion, then diverges for $\beta\mu > \pi$. Of course, Eq. (4.9) can immediately be used for a finite-density expansion in $\beta\mu$ to any order. It is also straightforwardly applicable to the case of imaginary chemical potential where all convergence issues are absent.

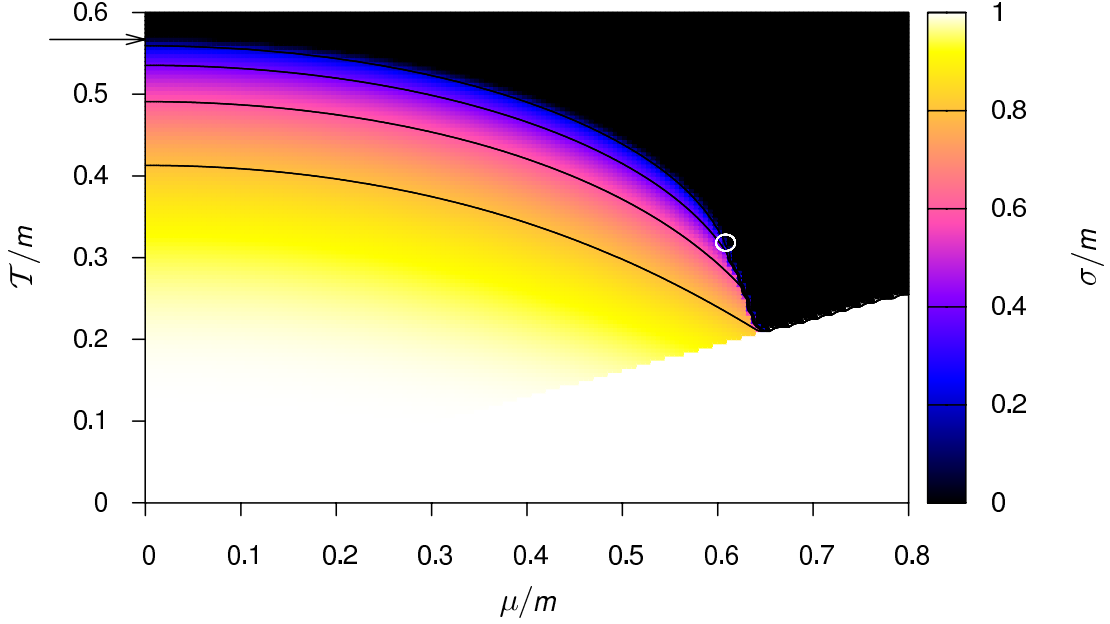


Figure 12: Phase diagram for a constant potential (cf. [63]) computed by numerically minimising the full action with respect to σ . The colour corresponds to the resulting σ value, the phase of restored chiral symmetry is in black. The tricritical point is marked by a white circle, located between phase transitions of second order (the upper boundary of the blue region) and transitions of first order (discrete jump of the colour/ σ value). The line of second order transitions extends to the $\mu = 0$ axis, where it is marked by an arrow at the value $\mathcal{T}_c \approx 0.567$ Eq. (4.4). The blank region below the $T = \mu/\pi$ line is inaccessible to the given expression for the action as discussed in the text.

As an application of Eq. (4.9), let us briefly revisit the phase diagram for a homogeneous σ condensate. The worldline expectation value for this is trivial, since $\exp(-\int V_{\pm}) = \exp(-T\sigma^2)$, for any single worldline. This case serves as a simple but instructive test for the (non-worldline) numerics of our algorithms, and for the representation Eq. (4.9). In Fig. 12, the phase diagram obtained by numerically minimising the full action with respect to σ for a given chemical potential and temperature is shown. In the accessible domain, that is for $\beta\mu < \pi$, the diagram agrees with the result of [63], as it should. At $\mu = 0$, we recover the critical temperature in Eq. (4.4). Even close to the line $\beta\mu = \pi$, i.e. temperature $\mathcal{T} = \mu/\pi$, below which the proper time integral has convergence problems, we obtain a stable result.

4.3 High densities and low temperatures

Let us further investigate the instability for $\beta\mu > \pi$. For this purpose, we first address the homogeneous background $\sigma = \text{constant}$, $\Phi[\sigma] = 1$, and extend the findings to the general case at the end of this subsection.

The (regularized) effective action is given by

$$\Gamma_{\beta,\mu} = \frac{1}{2} \int d^D x \frac{N_f d_\gamma}{(4\pi)^{D/2}} \int_{1/\Lambda^2}^{\infty} \frac{dT}{T^{1+D/2}} \left(\sum_{n=-\infty}^{\infty} (-1)^n e^{-\frac{\beta^2 n^2}{4T}} e^{-\mu\beta n} \right) e^{-T\sigma^2}. \quad (4.10)$$

In order to perform the sum over the windings n , we introduce a Hubbard-Stratonovich transformation by

$$(-1)^n e^{-\frac{\beta^2 n^2}{4T}} e^{-\mu \beta n} = \sqrt{\frac{4\pi T}{\beta^2}} \int d\nu e^{i2\pi n \nu} e^{-T[\frac{2\pi}{\beta}(\nu + \frac{1}{2}) - i\mu]^2}. \quad (4.11)$$

Inserting (4.11) in (4.10) yields for the T integral

$$\Gamma_{\beta, \mu} = \frac{1}{2} \int d^D x \frac{N_f d_\gamma}{(4\pi)^{D/2}} \int_{1/\Lambda^2}^\infty \frac{dT}{T^{1+D/2}} \sqrt{\frac{4\pi T}{\beta^2}} \sum_{n=-\infty}^\infty \int d\nu e^{i2\pi n \nu} e^{-T[\frac{2\pi}{\beta}(\nu + \frac{1}{2}) - i\mu]^2} e^{-T\sigma^2}. \quad (4.12)$$

The IR problem for large values T has become apparent: the T integration converges provided

$$\text{Re} \left[\left(\frac{\pi}{\beta} - i\mu \right)^2 + \sigma^2 \right] > 0. \quad (4.13)$$

For imaginary chemical potential this condition is always satisfied. But for real chemical potential we find the condition

$$\beta\mu < \sqrt{\pi^2 + \beta^2 \sigma^2}. \quad (4.14)$$

Allowing for the possibility of a vanishing condensate, or in the more general case for the existence of a zero mode in the spectrum, we restrict to chemical potentials satisfying the bound

$$\beta\mu < \pi. \quad (4.15)$$

The basic idea of the present subsection is to consider the case (4.15), then to derive an analytic expression for the effective action, and to perform an analytic continuation to values $\mu > \pi/\beta$. For a homogeneous background, we find that this approach recovers the well-known result familiar from solid state physics.

Hence, let us confine ourselves to values μ satisfying (4.15), and perform the T integration first. For this purpose, we introduce the “density of states” ρ_0 by

$$\frac{1}{T^{(D-1)/2}} e^{-T\sigma^2} = 2(4\pi)^{(D-1)/2} \int_0^\infty dE E \rho_0(E) e^{-TE^2}, \quad (4.16)$$

$$\rho_0(E) = \int \frac{d^{D-1}k}{(2\pi)^{D-1}} \delta(E^2 - \sigma^2 - k^2). \quad (4.17)$$

Rearranging (4.12) with the help of (4.16-4.17) yields

$$\Gamma_{\beta, \mu} = N_f d_\gamma \int d^D x \int_0^\infty dE E \rho_0(E) \frac{1}{\beta} \sum_{n=-\infty}^\infty \int_{1/\Lambda^2}^\infty \frac{dT}{T} \int d\nu e^{i2\pi n \nu} e^{-T[\frac{2\pi}{\beta}(\nu + \frac{1}{2}) - i\mu]^2} e^{-TE^2}. \quad (4.18)$$

The n sum, the ν integral, and the proper time integration can be performed in closed form. The details of this calculation are presented in appendix C. The final result is:

$$\begin{aligned} \Gamma_{\beta, \mu} &= \Gamma_{\infty, 0} \\ &- \frac{N_f d_\gamma}{\beta} \int d^D x \int_0^\infty dE E \rho_0(E) \left[\ln \left(1 + e^{-\beta(E-\mu)} \right) + \ln \left(1 + e^{-\beta(E+\mu)} \right) \right]. \end{aligned} \quad (4.19)$$

which we recognize as the standard expression [64]. Although this result was derived under the assumption (4.15), the closed form (4.19) is perfectly valid for $\beta\mu > \pi$. Hence, we perform an analytic continuation by taking (4.19) as the primary expression and consider the arbitrary values for $\beta\mu$ in the following.

Let us generalize the above findings to the more general case of a spatially dependent background field:

$$\Gamma_{\beta,\mu} = \frac{1}{2} \int d^D x \frac{N_f d_\gamma}{(4\pi)^{D/2}} \int_{1/\Lambda^2}^{\infty} \frac{dT}{T^{1+D/2}} \left(\sum_{n=-\infty}^{\infty} (-1)^n e^{-\frac{\beta^2 n^2}{4T}} e^{-\mu\beta n} \right) \left\langle e^{-\int_0^T d\tau \sigma^2} \Phi[\sigma] \right\rangle. \quad (4.20)$$

The key observation is that we can relate the general case (4.20) to the free case by defining the density of states $\rho(E)$ by

$$\frac{1}{T^{(D-1)/2}} \left\langle e^{-\int_0^T d\tau \sigma^2} \Phi[\sigma] \right\rangle = 2(4\pi)^{(D-1)/2} \int_0^{\infty} dE E \rho(E) e^{-TE^2}, \quad (4.21)$$

The final answer for the effective action $\Gamma_{\beta,\mu}$ is given by (4.19) where we replace ρ_0 by ρ from (4.21). Note that the left-hand side of (4.21) is only known numerically for real values T . The quite challenging task is then to perform the inverse Laplace transform to obtain $\rho(E)$. We however point out that, depending on the parameters, the full range of $\rho(E)$ is not needed. Let us consider the particle density $n_{\beta,\mu}$ for the moment ($V = \int d^D x$),

$$n_{\beta,\mu} = -\frac{1}{V} \frac{\partial \Gamma_{\beta,\mu}}{\partial \mu} = N_f d_\gamma \int_0^{\infty} dE E \rho(E) \left[\frac{1}{e^{\beta(E-\mu)} + 1} - \frac{1}{e^{\beta(E+\mu)} + 1} \right]. \quad (4.22)$$

For small temperatures, i.e., for $\beta\mu \gg 1$, we obtain the result (valid if μ lies within a band):

$$n_{\beta,\mu} = N_f d_\gamma \left\{ \int_0^{\mu} dE E \rho(E) + \frac{\pi^2}{6\beta^2} \frac{d}{dE} [E\rho(E)] \Big|_{E=\mu} + \mathcal{O}(1/\beta^4) \right\}. \quad (4.23)$$

In this case, the density of states need only be known for $E \lesssim \mu$.

4.4 Crystalline phase on the worldline

The crystalline phase of the GN model extends up to the tricritical point plotted in Fig. (12) [28]. This point and therewith some part of the crystalline phase is above the line defined by $\beta\mu = \pi$, where $\beta\mu > \pi$. Consequently, already the straight forward evaluation of Eq. (4.9) allows for studying translational-symmetry breaking.

We consider several points on a line slightly above the $\beta\mu = \pi$ line, given by $1.1\beta\mu = \pi$, which intersects the crystalline phase between $\mu = 0.63m$ and $\mu = 0.67m$. For each point, we determine the potential σ of the ground state analytically as described in [30]. Using this potential, we evaluate Eq. (2.18) and Eq. (4.9) with worldline numerics and compare the resulting value of the grand potential per volume with the corresponding value for the constant field solution.

Figure (13) shows the difference of these two values as well as the analytic result according to [30]. Both results agree nicely. In particular, the worldline numerical result

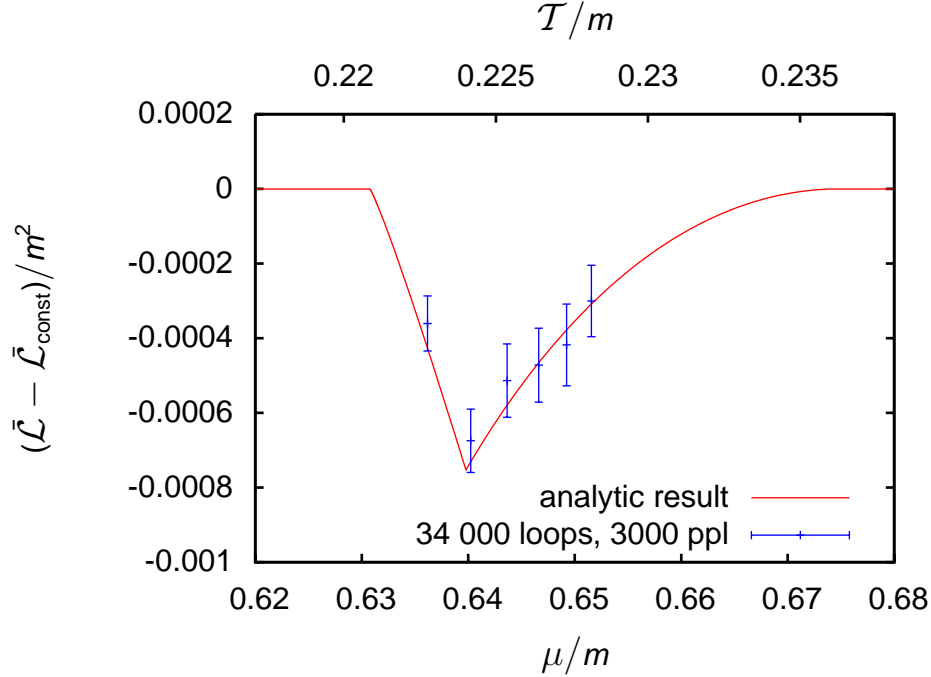


Figure 13: Difference between the grand potential per volume for the crystal and the homogeneous solution for $T = 1.1\mu/\pi$. The solid line is the analytic result from [30], the crosses with error bars are worldline numerical values. The line $T = 1.1\mu/\pi$ crosses the crystal phase between $\mu = 0.63m$ and $0.67m$, approximately. Consequently, we obtain negative values in this range. The numerical values agree with the analytic result and are significantly below zero.

confirms the thermodynamic preference of the crystal solution over the homogeneous potential in the range $0.63m < \mu < 0.67m$ which is reflected in negative values of the plotted difference.

5. Conclusions

We have demonstrated that the Monte Carlo approach to the worldline formulation of quantum field theory may be consistently implemented to study interacting fermionic models such as the Gross-Neveu model. We have explained the required formalism and tested numerically the worldline results in comparison to a number of analytic results for inhomogeneous condensates, pointing out the advantages and disadvantages of the numerical approach. In particular, in Section 4.4 we have used this approach to confirm the existence of the inhomogeneous crystalline phase of the Gross-Neveu model. While this is a highly non-trivial test, the true potential of the worldline Monte Carlo approach lies in the possibility of scaling up to higher dimensions without dramatic numerical problems, and the possibility of realizing chiral symmetries directly. These issues are under investigation.

Acknowledgments

KL thanks Simon Hands for helpful discussions on dense fermionic systems. GD thanks the

DOE for support through grant DE-FG02-92ER40716, and the DFG for support through a Mercator Professor Award held at Heidelberg in 2007, when this work was begun. HG acknowledges support by the DFG under contract Gi 328/1-4 (Emmy-Noether program) and Gi 328/5-1 (Heisenberg-Program). The work of KK was supported in part by the National Science Foundation under Grant No. PHY05-51164.

A. Fermionic models and continuous chiral symmetry

In this work, we have mainly focussed on the the $D = 1 + 1$ dimensional Gross-Neveu (GN) model defined by the Euclidean fermionic action in (2.1). The GN model has a discrete chiral symmetry under $\psi \rightarrow \gamma_5 \psi$, rather than a continuous chiral symmetry. In order to discuss the fate of chiral symmetry in our numerical worldline approach, it is instructive to study the Thirring model, defined by the action

$$S_F = \int d^D x \left(-\bar{\psi} \not{\partial} \psi + \frac{g^2}{2N_f} (\bar{\psi} \gamma_\mu \psi)^2 \right), \quad (\text{A.1})$$

In addition to global phase and axial rotations, the Thirring model is invariant under $SU(N_f)_R \times SU(N_f)_L$ chiral transformations. By means of a Hubbard-Stratonovich transformation, the model can be rewritten with the aid of a vector boson V_μ

$$S_{FB} = \int d^D x \left[\frac{N_f}{2g^2} V_\mu^2 - \bar{\psi} \not{\partial} \psi - i V_\mu \bar{\psi} \gamma_\mu \psi \right], \quad (\text{A.2})$$

where V_μ is invariant under chiral transformations. In the large- N_f limit, the effective action upon integrating out the fermion fluctuations yields

$$\Gamma[V_\mu] = \int d^D x \frac{N_f}{2g^2} V_\mu^2 - N_f \text{Tr} \ln(-\not{\partial} - i \not{V}), \quad N_f \rightarrow \infty. \quad (\text{A.3})$$

As in the Gross-Neveu case, the resulting Dirac operator $\mathcal{D} = i \not{\partial} - \not{V}$ has a γ_5 hermiticity, $\mathcal{D}^\dagger = \gamma_5 \mathcal{D} \gamma_5$, implying that Γ can be written as

$$\Gamma[V_\mu] = \int d^D x \frac{N_f}{2g^2} V_\mu^2 - \frac{N_f}{2} \text{Tr} \ln \left(-D[V]^2 + \frac{1}{2} \sigma_{\mu\nu} V_{\mu\nu} \right), \quad N_f \rightarrow \infty, \quad (\text{A.4})$$

where $D[V] = \partial_\mu + i V_\mu$, $\sigma_{\mu\nu} = \frac{i}{2} [\gamma_\mu, \gamma_\nu]$, and the vector field strength $V_{\mu\nu} = \partial_\mu V_\nu - \partial_\nu V_\mu$. By virtue of the $D = 1 + 1$ dimensional Dirac algebra, the spin-field coupling (Pauli term) can also be expressed as $\sigma_{\mu\nu} V_{\mu\nu} = \gamma_5 \epsilon_{\mu\nu} V_{\mu\nu} \equiv \gamma_5 \tilde{V}$. Here, we prefer to work with the representation given in Eq. (A.4) which generalizes straightforwardly to higher dimensions³. Note that the fermionic contribution exhibits an accidental local gauge symmetry, which is, however, not respected by the classical action $\sim V_\mu^2$.

Incidentally, the 4-fermion vector interaction of the Thirring model is the only $SU(N_f)_R \times SU(N_f)_L$ chirally invariant and parity-even interaction which contributes to leading-order

³Odd dimensions require reducible representations of the Dirac algebra in order to maintain γ_5 hermiticity of the Dirac operator.

at large- N_f in $D = 2$. In higher dimensions, also independent axial-vector interactions exist which, in $D = 2$, are isomorphic to the vector interaction.

The worldline representation for the Thirring model is well known from the analogous QED case. Concentrating on the contributions from the fermion fluctuations, we obtain

$$\begin{aligned}\Delta\Gamma[V] &:= -\frac{N_f}{2}\text{Tr}\ln\left(-D[V]^2 + \frac{1}{2}\sigma_{\mu\nu}F_{\mu\nu}\right) \\ &= \frac{N_f}{2}\frac{1}{(4\pi)^{D/2}}d_\gamma\int_{1/\Lambda^2}^{\infty}\frac{dT}{T^{D/2+1}}\int_{x(0)=x(T)}\mathcal{D}x e^{-\frac{1}{4}\int_0^T d\tau \dot{x}^2(\tau)} e^{-i\oint dx_\mu V_\mu}\Phi[V],\end{aligned}\quad (\text{A.5})$$

where the spin factor this time reads

$$\Phi[V] = \frac{1}{d_\gamma}\text{tr}_\gamma \mathcal{P}\exp\left(-\frac{1}{2}\int_0^T d\tau \sigma_{\mu\nu}V_{\mu\nu}\right). \quad (\text{A.6})$$

B. Exact resolvents and propagators for $(1+1)$ -dim. Gross-Neveu model

In this Appendix, we present the derivation of the exact expressions for $\langle e^{-\int_0^T d\tau V_\pm} \rangle$ discussed in Section 3, where they were also compared to our numerical worldline results. We compute, for various forms of the static condensate function $\sigma(x)$, the worldline propagators

$$K_\pm(x;T) \equiv \langle x|e^{-H_\pm T}|x\rangle \equiv \frac{1}{\sqrt{4\pi T}}\langle e^{-\int_0^T d\tau V_\pm} \rangle, \quad (\text{B.1})$$

where the Schrödinger-like Hamiltonian operators H_\pm are

$$H_\pm \equiv -\partial_x^2 + V_\pm(x) = -\partial_x^2 + \sigma^2(x) \pm \sigma'(x). \quad (\text{B.2})$$

Our strategy is to consider the associated "diagonal resolvents" [i.e., coincident-point Green's functions], which are Laplace transforms of the propagators:

$$R_\pm(x;-\lambda) \equiv \langle x|\frac{1}{H_\pm + \lambda}|x\rangle = \int_0^\infty dT e^{-\lambda T}\langle x|e^{-H_\pm T}|x\rangle. \quad (\text{B.3})$$

For *any* static condensate function $\sigma(x)$, the resolvent must satisfy the Gel'fand-Dik'ii equation [65]

$$-2R R'' + (R')^2 + 4R^2(V + \lambda) = 1, \quad (\text{B.4})$$

or its third-order linear form [obtained by differentiating (B.4)]

$$R''' - 4R'(V + \lambda) - 2RV' = 0 \quad (\text{B.5})$$

This identity follows directly from the fact that the Green's function in 1 dimension can be written in terms of the product of two independent solutions, and the product of two solutions necessarily satisfies such an equation. For details, see [65].

For certain special forms of static condensate $\sigma(x)$, these Gel'fand-Dik'ii equations are analytically soluble. Then $K_\pm(x;T)$ is obtained as the inverse Laplace transform of $R_\pm(T;-\lambda)$. Let us consider several examples:

B.1 Homogeneous condensate

With a homogeneous condensate $\sigma(x) = m$, we have $V_{\pm} = m^2$, so that solving (B.4)–(B.5) leads to

$$R_{\pm}(x; -\lambda) = \frac{1}{2\sqrt{m^2 + \lambda}} \quad . \quad (\text{B.6})$$

It is straightforward to take the inverse Laplace transform to arrive at the free propagator in (3.6).

B.2 Single kink condensate

Consider the inhomogeneous kink-like condensate $\sigma(x) = A \tanh(Ax)$, for which

$$V_{\pm} = \begin{cases} A^2 \\ A^2(1 - 2 \operatorname{sech}^2(Ax)) \end{cases} \quad (\text{B.7})$$

Then $R_{\pm}(x; -\lambda)$ can be obtained from (B.4)–(B.5) by substituting the *ansatz* form

$$R_{\pm}(x; -\lambda) = \alpha_{\pm}(\lambda) + \beta_{\pm}(\lambda) \operatorname{sech}^2(Ax) \quad , \quad (\text{B.8})$$

and solving algebraically for the $[\lambda\text{-dependent}]$ coefficients α_{\pm} and β_{\pm} . A simple calculation leads to

$$R_{\pm}(x; -\lambda) = \begin{cases} \frac{1}{2\sqrt{A^2 + \lambda}} \\ \frac{1}{2\sqrt{A^2 + \lambda}} \left(1 + \frac{A^2}{\lambda} \operatorname{sech}^2(Ax) \right) \end{cases} \quad . \quad (\text{B.9})$$

The corresponding propagators follow from the inverse Laplace transform, and are presented in (3.12).

B.3 Kink-antikink pair condensate

Consider the inhomogeneous condensate corresponding to a kink-antikink pair

$$\begin{aligned} \sigma(x) &= A (\coth(b) + [\tanh(Ax) - \tanh(Ax + b)]) \\ &= A ([\coth(b) - \tanh(b)] + \tanh(b) \tanh(Ax) \tanh(Ax + b)) \quad . \end{aligned} \quad (\text{B.10})$$

The corresponding potentials are

$$V_{\pm} = A^2 \left(\coth^2(b) - 2 \left\{ \frac{\operatorname{sech}^2(Ax + b)}{\operatorname{sech}^2(Ax)} \right\} \right) \quad . \quad (\text{B.11})$$

The resolvents can be derived by similar ansatze to (B.8), using $\operatorname{sech}^2(Ax + b)$ for V_+ , and $\operatorname{sech}^2(Ax)$ for V_- . This leads straightforwardly to

$$R_{\pm}(x; -\lambda) = \frac{1}{2\sqrt{A^2 \coth^2(b) + \lambda}} \left(1 + \frac{A^2}{\frac{A^2}{\sinh^2(b)} + \lambda} \left\{ \frac{\operatorname{sech}^2(Ax + b)}{\operatorname{sech}^2(Ax)} \right\} \right) \quad (\text{B.12})$$

The propagators again follow from the inverse Laplace transform, and are presented in (3.15).

B.4 Periodic array of kink-antikink pairs

Consider the condensate formed by a periodic array of kink-antikink pairs

$$\begin{aligned}\sigma(x) &= A \left(\left[Z(b; \nu) + \frac{\text{cn}(b; \nu) \text{dn}(b; \nu)}{\text{sn}(b; \nu)} \right] + [Z(Ax; \nu) - Z(Ax + b; \nu)] \right) \\ &= A \left(\frac{\text{cn}(b; \nu) \text{dn}(b; \nu)}{\text{sn}(b; \nu)} + \nu \text{sn}(b; \nu) \text{sn}(Ax; \nu) \text{sn}(Ax + b; \nu) \right) .\end{aligned}\quad (\text{B.13})$$

The potentials corresponding to the periodic condensate (B.13) are

$$V_{\pm} = A^2 \left(\frac{1}{\text{sn}^2(b; \nu)} - 1 + \nu - 2\nu \left\{ \frac{\text{cn}^2(Ax + b; \nu)}{\text{cn}^2(Ax; \nu)} \right\} \right) . \quad (\text{B.14})$$

The resolvents for V_{\pm} can be obtained by substituting ansatze as in (B.8), but with sech^2 replaced by cn^2 , and with the argument shifted by b in the case of V_+ . Straightforward algebra yields

$$\begin{aligned}R_{\pm}(x; -\lambda) &= \\ &= \frac{\sqrt{A^2 \text{ds}^2(b; \nu) + \lambda}}{2\sqrt{A^2 \text{cs}^2(b; \nu) + \lambda} \sqrt{A^2 \text{ns}^2(b; \nu) + \lambda}} \left(1 + \frac{A^2 \nu}{A^2 \text{ds}^2(b; \nu) + \lambda} \left\{ \frac{\text{cn}^2(Ax + b; \nu)}{\text{cn}^2(Ax; \nu)} \right\} \right) .\end{aligned}\quad (\text{B.15})$$

The propagators again follow from the inverse Laplace transform, and are presented in (3.21). The kink crystal case, where the antikinks lie at the edges of the period, is obtained by the simple substitution $b \rightarrow K(\nu)$.

B.5 Comparison with heat kernel expansion

It is instructive to compare the exact transition amplitudes, or heat kernels, not only with our numerical worldline loop results, but also with the approximate small T heat kernel expansions [66, 67, 68]. In general, the transition amplitude/heat kernel has an asymptotic small T expansion

$$K(x; T) \sim \frac{1}{\sqrt{4\pi T}} \sum_{n=0}^{\infty} b_n(x) T^n , \quad (\text{B.16})$$

where the functionals $b_n(x)$ are expressed in terms of the potential and its derivatives, and are given by:

$$\begin{aligned}b_0(x) &= 1 \\ b_1(x) &= -V \\ b_2(x) &= \frac{1}{2} \left(V^2 - \frac{1}{3} V'' \right) \\ b_3(x) &= -\frac{1}{6} \left(V^3 - \frac{1}{2} (V')^2 - V V'' + \frac{1}{10} V'''' \right) \\ &\vdots\end{aligned}\quad (\text{B.17})$$

Defining $b_n(x) = \frac{2^{n+1}}{(2n-1)!!} r_n(x)$, the r_n are given recursively by :

$$r_n = \frac{1}{2} \sum_{k=0}^{n-2} r_k r''_{n-k-1} - \frac{1}{4} \sum_{k=1}^{n-2} r'_k r'_{n-k-1} - V \sum_{k=0}^{n-1} r_k r_{n-k-1} - \sum_{k=1}^{n-1} r_k r_{n-k} \quad , \quad (\text{B.18})$$

with $r_0 = \frac{1}{2}$ and $r_1 = -\frac{1}{4}V$.

For example, for the single-kink condensate, with $V_- = A^2 (1 - 2 \operatorname{sech}^2(Ax))$, the heat kernel expansion (B.16) is

$$K_-(x; T) = \frac{1}{\sqrt{4\pi T}} \left\{ 1 - A^2 T [1 - 2 \operatorname{sech}^2(Ax)] + \frac{1}{2} A^4 T^2 \left[1 - \frac{4}{3} \operatorname{sech}^2(Ax) \right] - \frac{1}{6} A^6 T^3 \left[1 - \frac{6}{5} \operatorname{sech}^2(Ax) \right] + \dots \right\} \quad , \quad (\text{B.19})$$

in agreement with the small T expansion of the exact result in (3.12). This comparison is made in the first plot of Figure 2. Similarly, for the periodic kink-antikink condensate, with $V_-(x)$ as in (B.14), the heat kernel expansion (B.16) is

$$K_-(x; T) = \frac{1}{\sqrt{4\pi T}} \left\{ 1 - A^2 T \left[\nu - 1 + \frac{1}{\operatorname{sn}^2(b; \nu)} - 2\nu \operatorname{cn}^2(Ax; \nu) \right] + \frac{1}{2} A^4 T^2 \left[\frac{(1-\nu)(\nu+3)}{3} + \frac{2(\nu-1)}{\operatorname{sn}^2(b; \nu)} + \frac{1}{\operatorname{sn}^4(b; \nu)} - \left(\frac{4\nu}{\operatorname{sn}^2(b; \nu)} - \frac{4}{3} \nu(\nu+1) \right) \operatorname{cn}^2(Ax; \nu) \right] + \dots \right\} \quad , \quad (\text{B.20})$$

in agreement with the small T expansion of the exact result in (3.21). This comparison is made in Figure 7.

C. Effective action for the homogeneous case

This section provides detailed information on the evaluation of the integrals and sums which appear in the effective action (4.18) for a homogeneous background field. We firstly focus on the contributions from the terms with $n \neq 0$:

$$I(E) = \frac{1}{\beta} \sum_{n \neq 0} \int_0^\infty \frac{dT}{T} \int d\nu e^{i2\pi n \nu} e^{-T[\frac{2\pi}{\beta}(\nu + \frac{1}{2}) - i\mu]^2} e^{-TE^2} \quad . \quad (\text{C.1})$$

Let us first perform the proper time integration. Using the identity

$$2 \int_E^\infty dx x e^{-Tx^2} = \frac{1}{T} e^{-TE^2} \quad , \quad (\text{C.2})$$

the T integration can be performed:

$$I(E) = \frac{2}{\beta} \int_E^\infty dx x \sum_{n \neq 0} \int d\nu e^{i2\pi n \nu} \frac{1}{[\frac{2\pi}{\beta}(\nu + \frac{1}{2}) - i\mu]^2 + x^2} \quad . \quad (\text{C.3})$$

The ν integration requires to distinguish the cases $x > \mu$ and $x < \mu$, but can otherwise be straightforwardly done using the Cauchy integral theorem:

$$I(E) = \int_E^\infty dx \sum_{n=1}^\infty (-1)^n \left[e^{-\beta n(x+\mu)} + \text{sign}(x-\mu) e^{-\beta n|x-\mu|} \right]. \quad (\text{C.4})$$

The geometric series in n can easily be summed:

$$I(E) = - \int_E^\infty dx \left[\frac{e^{-\beta(x+\mu)}}{1 + e^{-\beta(x+\mu)}} + \text{sign}(x-\mu) \frac{e^{-\beta|x-\mu|}}{1 + e^{-\beta|x-\mu|}} \right]. \quad (\text{C.5})$$

Using the identity

$$\frac{e^{-\beta(\mu-x)}}{1 + e^{-\beta(\mu-x)}} = 1 - \frac{e^{-\beta(x-\mu)}}{1 + e^{-\beta(x-\mu)}},$$

the expression (C.5) can be written as

$$I(E) = - \int_E^\infty dx \left[\frac{e^{-\beta(x+\mu)}}{1 + e^{-\beta(x+\mu)}} - \theta(\mu-x) + \frac{e^{-\beta(x-\mu)}}{1 + e^{-\beta(x-\mu)}} \right]. \quad (\text{C.6})$$

Let us now consider the contribution with zero winding $n = 0$ in Eq. (4.18):

$$I_0(E, \mu) = \frac{1}{\beta} \int_{1/\Lambda^2}^\infty \frac{dT}{T} \int d\nu e^{-T[\frac{2\pi}{\beta}(\nu+\frac{1}{2})-i\mu]^2} e^{-TE^2}. \quad (\text{C.7})$$

It is convenient to decompose the latter expression as

$$I_0(E, \mu) = \Delta I_0(E, \mu) + I_0(E, 0), \quad (\text{C.8})$$

$$\Delta I_0(E, \mu) = \frac{1}{\beta} \int_0^\infty \frac{dT}{T} e^{-TE^2} \int d\nu \left[e^{-T[\frac{2\pi}{\beta}(\nu+\frac{1}{2})-i\mu]^2} - e^{-T[\frac{2\pi}{\beta}(\nu+\frac{1}{2})]^2} \right]. \quad (\text{C.9})$$

Note that the latter expression is UV finite. We have therefore removed the regulator by taking the limit $\Lambda \rightarrow \infty$. A direct calculation of $\Delta I_0(E, \mu)$ along the same lines outlined above yields

$$\Delta I_0(E, \mu) = - \int_E^\infty dx \theta(\mu-x). \quad (\text{C.10})$$

Thus, combining (C.6) and (C.7) gives

$$I(E) + I_0(E, \mu) = I_0(E, 0) - \int_E^\infty dx \left[\frac{e^{-\beta(x+\mu)}}{1 + e^{-\beta(x+\mu)}} + \frac{e^{-\beta(x-\mu)}}{1 + e^{-\beta(x-\mu)}} \right]. \quad (\text{C.11})$$

The final integration can easily be done leaving us with

$$I(E) + I_0(E, \mu) = I_0(E, 0) - \frac{1}{\beta} \left[\ln \left(1 + e^{-\beta(E-\mu)} \right) + \ln \left(1 + e^{-\beta(E+\mu)} \right) \right]. \quad (\text{C.12})$$

References

- [1] M. A. Stephanov, “QCD phase diagram: An overview,” PoS **LAT2006**, 024 (2006) [arXiv:hep-lat/0701002].
- [2] S. Choe *et al.*, “Responses of hadrons to the chemical potential at finite temperature,” Phys. Rev. D **65**, 054501 (2002).
- [3] C. R. Allton *et al.*, “The QCD thermal phase transition in the presence of a small chemical potential,” Phys. Rev. D **66**, 074507 (2002) [hep-lat/0204010].
- [4] S. Ejiri, C. R. Allton, S. J. Hands, O. Kaczmarek, F. Karsch, E. Laermann and C. Schmidt, “Study of QCD thermodynamics at finite density by Taylor expansion,” Prog. Theor. Phys. Suppl. **153**, 118 (2004) [hep-lat/0312006].
- [5] M. G. Alford, A. Kapustin and F. Wilczek, “Imaginary chemical potential and finite fermion density on the lattice,” Phys. Rev. D **59**, 054502 (1999) [hep-lat/9807039].
- [6] P. de Forcrand and O. Philipsen, “The QCD phase diagram for small densities from imaginary chemical potential,” Nucl. Phys. B **642**, 290 (2002) [hep-lat/0205016].
- [7] M. D’Elia and M. P. Lombardo, “Finite density QCD via imaginary chemical potential,” Phys. Rev. D **67**, 014505 (2003) [hep-lat/0209146].
- [8] Z. Fodor and S. D. Katz, “A new method to study lattice QCD at finite temperature and chemical potential,” Phys. Lett. B **534**, 87 (2002) [hep-lat/0104001]; “Lattice determination of the critical point of QCD at finite T and μ ,” JHEP **0203**, 014 (2002) [hep-lat/0106002]; “Critical point of QCD at finite T and μ , lattice results for physical quark masses,” JHEP **0404**, 050 (2004) [hep-lat/0402006].
- [9] S. Hands, J. B. Kogut, M. P. Lombardo and S. E. Morrison, “Symmetries and spectrum of SU(2) lattice gauge theory at finite chemical potential,” Nucl. Phys. B **558**, 327 (1999) [hep-lat/9902034].
- [10] J. B. Kogut, D. Toublan and D. K. Sinclair, “The phase diagram of four flavor SU(2) lattice gauge theory at nonzero chemical potential and temperature,” Nucl. Phys. B **642**, 181 (2002) [hep-lat/0205019].
- [11] S. Hands, S. Kim and J. I. Skullerud, “Deconfinement in dense 2-color QCD,” Eur. Phys. J. C **48**, 193 (2006) [hep-lat/0604004].
- [12] D. Bailin and A. Love, “Superfluidity And Superconductivity In Relativistic Fermion Systems,” Phys. Rept. **107**, 325 (1984).
- [13] M. G. Alford, K. Rajagopal and F. Wilczek, “QCD at finite baryon density: Nucleon droplets and color superconductivity,” Phys. Lett. B **422**, 247 (1998) [hep-ph/9711395].
- [14] T. Schafer and F. Wilczek, “Superconductivity from perturbative one-gluon exchange in high density quark matter,” Phys. Rev. D **60**, 114033 (1999) [hep-ph/9906512].
- [15] R. D. Pisarski and D. H. Rischke, “Color superconductivity in weak coupling,” Phys. Rev. D **61**, 074017 (2000) [nucl-th/9910056].
- [16] M. G. Alford, A. Schmitt, K. Rajagopal and T. Schafer, “Color superconductivity in dense quark matter,” Rev. Mod. Phys. **80**, 1455 (2008) [arXiv:0709.4635 [hep-ph]].
- [17] M. G. Alford, J. A. Bowers and K. Rajagopal, “Crystalline color superconductivity,” Phys. Rev. D **63**, 074016 (2001) [arXiv:hep-ph/0008208].

- [18] K. Rajagopal and F. Wilczek, “The condensed matter physics of QCD,” arXiv:hep-ph/0011333.
- [19] J. A. Bowers and K. Rajagopal, “The crystallography of color superconductivity,” Phys. Rev. D **66**, 065002 (2002) [arXiv:hep-ph/0204079].
- [20] R. Casalbuoni and G. Nardulli, “Inhomogeneous superconductivity in condensed matter and QCD,” Rev. Mod. Phys. **76**, 263 (2004) [arXiv:hep-ph/0305069].
- [21] I. R. Klebanov, “Nuclear Matter In The Skyrme Model,” Nucl. Phys. B **262**, 133 (1985).
- [22] A. S. Goldhaber and N. S. Manton, “Maximal Symmetry Of The Skyrme Crystal,” Phys. Lett. B **198**, 231 (1987).
- [23] A. D. Jackson and J. J. M. Verbaarschot, “Phase structure of the Skyrme model,” Nucl. Phys. A **484**, 419 (1988); L. Castillejo, P. S. J. Jones, A. D. Jackson, J. J. M. Verbaarschot and A. Jackson, “Dense Skyrmion Systems,” Nucl. Phys. A **501**, 801 (1989).
- [24] N. S. Manton and P. M. Sutcliffe, “Skyrme crystal from a twisted instanton on a four torus,” Phys. Lett. B **342**, 196 (1995) [arXiv:hep-th/9409182].
- [25] B. Rosenstein, B. Warr and S. H. Park, “Dynamical symmetry breaking in four Fermi interaction models,” Phys. Rept. **205**, 59 (1991).
- [26] S. Hands, A. Kocic and J. B. Kogut, “The Four Fermi Model In Three-Dimensions At Nonzero Density And Temperature,” Nucl. Phys. B **390**, 355 (1993) [arXiv:hep-lat/9206024].
- [27] F. Karsch, J. B. Kogut and H. W. Wyld, “The Gross-Neveu Model At Finite Temperature And Density,” Nucl. Phys. B **280**, 289 (1987).
- [28] M. Thies, “Analytical solution of the Gross-Neveu model at finite density,” Phys. Rev. D **69**, 067703 (2004) [arXiv:hep-th/0308164]; M. Thies and K. Urlichs, “Revised phase diagram of the Gross-Neveu model,” Phys. Rev. D **67**, 125015 (2003) [hep-th/0302092].
- [29] M. Thies, “From relativistic quantum fields to condensed matter and back again: Updating the Gross-Neveu phase diagram,” J. Phys. A **39**, 12707 (2006) [hep-th/0601049];
- [30] O. Schnetz, M. Thies and K. Urlichs, “Phase diagram of the Gross-Neveu model: Exact results and condensed matter precursors,” Annals Phys. **314** (2004) 425 [arXiv:hep-th/0402014].
- [31] G. Basar and G. V. Dunne, “Self-consistent crystalline condensate in chiral Gross-Neveu and Bogoliubov-de Gennes systems,” Phys. Rev. Lett. **100**, 200404 (2008) [arXiv:0803.1501 [hep-th]]; “A Twisted Kink Crystal in the Chiral Gross-Neveu model,” Phys. Rev. D **78**, 065022 (2008) [arXiv:0806.2659 [hep-th]]; G. Basar, G. V. Dunne and M. Thies, “Inhomogeneous Condensates in the Thermodynamics of the Chiral NJL_2 model,” arXiv:0903.1868 [hep-th].
- [32] P. de Forcrand and U. Wenger, “New baryon matter in the lattice Gross-Neveu model,” PoS **LAT2006**, 152 (2006) [arXiv:hep-lat/0610117].
- [33] B. Bringoltz, “Chiral crystals in strong-coupling lattice QCD at nonzero chemical potential,” JHEP **0703**, 016 (2007) [arXiv:hep-lat/0612010]; “Solving two-dimensional large-N QCD with a nonzero density of baryons and arbitrary quark mass,” arXiv:0901.4035 [hep-lat].

- [34] D. Nickel and M. Buballa, “Solitonic ground states in (color-) superconductivity,” arXiv:0811.2400 [hep-ph]; D. Nickel, “How many phases meet at the chiral critical point?,” arXiv:0902.1778 [hep-ph].
- [35] H. B. Nielsen and M. Ninomiya, “Absence Of Neutrinos On A Lattice. 1. Proof By Homotopy Theory,” Nucl. Phys. B **185**, 20 (1981) [Erratum-ibid. B **195**, 541 (1982)].
- [36] J. B. Kogut and L. Susskind, “Hamiltonian Formulation Of Wilson’s Lattice Gauge Theories,” Phys. Rev. D **11**, 395 (1975).
- [37] D. B. Kaplan, “A Method for simulating chiral fermions on the lattice,” Phys. Lett. B **288**, 342 (1992) [hep-lat/9206013].
- [38] H. Neuberger, “Exactly massless quarks on the lattice,” Phys. Lett. B **417**, 141 (1998) [hep-lat/9707022].
- [39] P. H. Ginsparg and K. G. Wilson, “A Remnant Of Chiral Symmetry On The Lattice,” Phys. Rev. D **25**, 2649 (1982).
- [40] C. Schubert, “Perturbative quantum field theory in the string-inspired formalism,” Phys. Rept. **355**, 73 (2001) [hep-th/0101036].
- [41] M. J. Strassler, “Field theory without Feynman diagrams: One loop effective actions,” Nucl. Phys. B **385**, 145 (1992) [arXiv:hep-ph/9205205].
- [42] H. Gies and K. Langfeld, “Quantum diffusion of magnetic fields in a numerical worldline approach,” Nucl. Phys. B **613**, 353 (2001) [hep-ph/0102185]; “Loops and loop clouds: A numerical approach to the worldline formalism in QED,” Int. J. Mod. Phys. A **17**, 966 (2002) [hep-ph/0112198].
- [43] H. Gies, K. Langfeld and L. Moyaerts, “Casimir effect on the worldline,” JHEP **0306**, 018 (2003) [hep-th/0303264].
- [44] H. Gies and K. Klingmuller, “Casimir effect for curved geometries: PFA validity limits,” Phys. Rev. Lett. **96**, 220401 (2006) [quant-ph/0601094]; “Worldline algorithms for Casimir configurations,” Phys. Rev. D **74**, 045002 (2006) [quant-ph/0605141]; “Casimir edge effects,” Phys. Rev. Lett. **97**, 220405 (2006) [quant-ph/0606235].
- [45] K. Langfeld, L. Moyaerts and H. Gies, “Fermion-induced quantum action of vortex systems,” Nucl. Phys. B **646**, 158 (2002) [hep-th/0205304].
- [46] G. V. Dunne and C. Schubert, “Worldline instantons and pair production in inhomogeneous fields,” Phys. Rev. D **72**, 105004 (2005) [hep-th/0507174]; G. V. Dunne, Q. h. Wang, H. Gies and C. Schubert, “Worldline instantons. II: The fluctuation prefactor,” Phys. Rev. D **73**, 065028 (2006) [hep-th/0602176].
- [47] H. Gies and K. Klingmuller, “Pair production in inhomogeneous fields,” Phys. Rev. D **72**, 065001 (2005) [hep-ph/0505099].
- [48] M. G. Schmidt and I. Stamatescu, “Matter Determinants In Background Fields Using Random Walk World Line Loops On The Lattice,” Mod. Phys. Lett. A **18**, 1499 (2003).
- [49] D. J. Gross and A. Neveu, “Dynamical Symmetry Breaking In Asymptotically Free Field Theories,” Phys. Rev. D **10**, 3235 (1974).
- [50] R. F. Dashen, B. Hasslacher and A. Neveu, “Semiclassical Bound States In An Asymptotically Free Theory,” Phys. Rev. D **12**, 2443 (1975).

- [51] H. Gies, J. Sanchez-Guillen and R. A. Vazquez, “Quantum effective actions from nonperturbative worldline dynamics,” JHEP **0508**, 067 (2005) [arXiv:hep-th/0505275].
- [52] K. Gawedzki and A. Kupiainen, “Renormalizing The Nonrenormalizable,” Phys. Rev. Lett. **55**, 363 (1985).
- [53] K. Langfeld, G. Dunne, H. Gies and K. Klingmuller, “Worldline Approach to Chiral Fermions,” PoS **LATTICE2007**, 202 (2006) [arXiv:0709.4595 [hep-lat]].
- [54] M. Abramowitz and I. Stegun, *Handbook of Mathematical Functions* (Dover, NY, 1970).
- [55] E. Whittaker and G. Watson, *Modern Analysis*, (Cambridge University Press, 1902).
- [56] S. A. Brazovskii, S. A. Gordynin, and N. N. Kirova, “Exact solution of the Peierls model with an arbitrary number of electrons in the unit cell”, Pis. Zh. Eksp. Teor. Fiz. **31**, 486 (1980) [JETP Lett. **31**, 456 (1980)]; “Excitons, polarons and bipolarons in conducting polymers”, Pis. Zh. Eksp. Teor. Fiz. **33**, 6 (1981) [JETP Lett. **33**, 4 (1981)]; S. A. Brazovskii, N. N. Kirova and Matveenko, “Peierls effect in conducting polymers”, Zh. Eksp. Teor. Fiz. **86**, 743 (1984) Sov. Phys. JETP **59**, 434 (1984).
- [57] B. Horovitz, “Soliton Lattice in Polyacetylene, Spin-Peierls Systems, and Two-Dimensional Sine-Gordon Systems”, Phys. Rev. Lett. **46**, 742 (1981).
- [58] J. Mertsching and H. J. Fischbeck, “The incommensurate Peierls phase of the quasi-dimensional Frohlich model with a nearly half-filled band”, Phys. Stat. Sol. B **103**, 783 (1981).
- [59] A. I. Buzdin and V. V. Tugushev, “Phase diagrams of electronic and superconducting transitions to soliton lattice states”, Zh. Eksp. Teor. Fiz. **85**, 735 (1983), [Sov. Phys. JETP **58**, 428 (1983)]; K. Machida and H. Nakanishi, “Superconductivity under a ferromagnetic molecular field”, Phys. Rev. B **30**, 122 (1984).
- [60] S. P. Novikov, “A periodic problem for the Korteweg-de Vries equations”, Funkts. Anal. i Prilozhen. **8**, 54 (1974); B. A. Dubrovin and S. P. Novikov, “Periodic and conditionally periodic analogues of the many soliton solutions of the Korteweg-de Vries equations, Zh. Eksp. Teor. Fiz. **67**, 2131 (1974).
- [61] G. V. Dunne and J. Feinberg, “Self-isospectral periodic potentials and supersymmetric quantum mechanics,” Phys. Rev. D **57**, 1271 (1998) [arXiv:hep-th/9706012].
- [62] K. Klingmuller and H. Gies, J. Phys. A **41**, 164042 (2008) [arXiv:0710.4473 [quant-ph]].
- [63] U. Wolff, “The Phase Diagram Of The Infinite N Gross-Neveu Model At Finite Temperature And Chemical Potential,” Phys. Lett. B **157**, 303 (1985).
- [64] J. I. Kapusta, *Finite Temperature Field Theory*, (Cambridge Univ. Press, 1989).
- [65] J. Feinberg, “All about the static fermion bags in the Gross-Neveu model,” Annals Phys. **309**, 166 (2004) [arXiv:hep-th/0305240].
- [66] P. B. Gilkey, *Invariance theory, the heat equation and the Atiyah-Singer index theorem*, (CRC Press, Boca Raton, 1995).
- [67] K. Kirsten, *Spectral functions in mathematics and physics*, (Chapman and Hall/CRC, Boca Raton, 2001).
- [68] D. V. Vassilevich, “Heat kernel expansion: User’s manual,” Phys. Rept. **388**, 279 (2003) [arXiv:hep-th/0306138].